

# Empirical Corrections for Charge Transfer Inefficiency and Associated Centroid Shifts for STIS CCD Observations<sup>1</sup>

Paul Goudfrooij, Ralph C. Bohlin, Jesús Maíz-Apellániz<sup>2,3</sup>

*Space Telescope Science Institute, 3700 San Martin Drive, Baltimore, MD 21218*

`goudfroo, bohlin, jmaiz@stsci.edu`

and

Randy A. Kimble

*NASA Goddard Space Flight Center, Code 667, Greenbelt, MD 20771*

`randy.a.kimble@nasa.gov`

## ABSTRACT

A variety of on-orbit imaging and spectroscopic observations are used to characterize the Charge Transfer Efficiency (CTE) of the Charge-Coupled Device (CCD) of the Space Telescope Imaging Spectrograph (STIS) aboard the *Hubble Space Telescope*. A set of formulae is presented to correct observations of point sources for CTE-related loss of signal. For data taken in imaging mode, the CTE loss is parametrized in terms of the location of the source on the CCD, the source signal level within the measurement aperture, the background level, and the time of observation. For spectroscopic data, it is found that one additional parameter is needed to provide an adequate calibration of the CTE loss, namely the signal in the point spread function located between the signal extraction box and the read-out amplifier. The effect of the latter parameter is significant for spectra taken using the G750L or G750M gratings of STIS. The algorithms presented

---

<sup>1</sup>Based on observations with the NASA/ESA *Hubble Space Telescope*, obtained at the Space Telescope Science Institute, which is operated by AURA, Inc., under NASA contract NAS5-26555.

<sup>2</sup>Affiliated with the Space Telescope Division, European Space Agency.

<sup>3</sup>Current Address: Instituto de Astrofísica de Andalucía, P. O. Box 3004, E-18080 Granada, Spain

here correct flux calibration inaccuracies due to CTE losses as large as 30% to within  $\sim 1.5\%$  RMS throughout the wavelength range covered by the STIS CCD modes. This uncertainty is similar to the Poisson noise associated with a source detected at a signal level of about 2500 electrons per resolution element. Using bi-directional CCD readouts, centroid shifts incurred due to CTE loss are also derived. A tight correlation is found between the CTE loss and the centroid shift (both for imaging and spectroscopic modes), thus enabling one to correct for both effects of imperfect charge transfer to STIS CCD observations.

*Subject headings:* instrumentation: detectors — methods: data analysis

## 1. Introduction

Astronomical observation was revolutionized about 25 years ago by charge-coupled device (CCD) technology, due to a combination of generally linear response over a very large dynamic range and high quantum efficiency. However, a shortcoming of CCDs is the fact that the transfer of charge from one pixel to the next is not perfect. Charge Transfer Efficiency (CTE) is the term commonly used to describe this effect, and it is quantified by the fraction of charge successfully moved (clocked) between adjacent pixels. In practice it is often more useful to use the term Charge Transfer *Inefficiency* ( $CTI \equiv 1 - CTE$ ). We will do so in this paper when considering quantitative measures. The main observational effect of CTE loss is that a star whose induced charge has to traverse many pixels before being read out appears to be fainter than the same star observed near the read-out amplifier.

Laboratory tests have shown that the CTE loss of CCDs increases significantly when being subjected to radiation damage (e.g., Janesick et al. 1991). This is particularly relevant for space-borne CCDs such as those aboard *Hubble Space Telescope (HST)*, where the flux of high-energy particles, particularly in the South Atlantic Anomaly, is significantly higher than on the ground. The effect is significant for all CCD detectors used on *HST* instruments (e.g., WFPC2: Whitmore, Heyer, & Casertano 1999; Dolphin 2000; STIS: Goudfrooij & Kimble 2003; ACS: Riess & Mack 2004), and charge losses increase with elapsed on-orbit time. The purpose of the current paper is to characterize the CTE loss of the CCD of the Space Telescope Imaging Spectrograph (STIS) for observations of point sources in terms of its dependencies on the X and Y positions, target intensity, background counts, measurement aperture size, observing mode, and elapsed on-orbit time. Several aspects of on-orbit characterizations of the CTE loss of the STIS CCD have been reported by Gilliland, Goudfrooij, & Kimble (1999), Kimble, Goudfrooij, & Gilliland (2000), Goudfrooij & Kimble (2003), and Bohlin & Goudfrooij (2003). The current paper provides

a comprehensive description of the final STIS CTE calibrations, using data taken through mid-2004 (i.e., just before STIS operations ended) which allows a more accurate temporal dependence of the CTE loss than the reports mentioned above. The current paper also includes analysis of data taken specifically to constrain the CTE loss at lower signal levels than before. Furthermore, we provide (for the first time) *(i)* separate characterizations of the CTE loss for spectroscopic and imaging modes, *(ii)* a comparison between data taken in gain = 1 and gain = 4 e<sup>-</sup> DN<sup>-1</sup> settings, and *(iii)* the relation of the CTE loss with its associated centroid shifts.

The STIS CCD is a 1024 × 1024 pixel, backside-illuminated device with 21 μm × 21 μm pixels. The CCD was built by Scientific Imaging Technology (SITE) with a coating process that allows coverage of the 200–1000 nm wavelength range for STIS in a wide variety of imaging and spectroscopic modes. Key features of the STIS CCD architecture are shown schematically in Figure 1. Two serial registers are available. A read-out amplifier is located at all four corners, each with an independent analog signal processing chain. The full image can be read out through any one of the four amplifiers, or through two- and four-amplifier combinations. By default, science exposures employ full-frame readout through amplifier ‘D’, which features the lowest read-out noise (4.0 e<sup>-</sup> RMS at launch).

Further technical details regarding the STIS CCD in particular are provided in Kimble et al. (1994), while background information on the design of STIS in general can be found in Woodgate et al. (1998).

This paper is organized as follows. Section 2 describes methods used to measure the CTE loss: Two methods designed to quantify different aspects of CTE loss for observations of point sources in sparse fields for spectroscopic and imaging modes, and one method to improve the characterization of the CTE loss for point source spectroscopy, using on-orbit observations of spectrophotometric standard stars. Section 3 presents the results of the CTE analyses, and Section 4 summarizes the results.

## 2. CTE Measurement Methods

### 2.1. Spectroscopic Modes

#### 2.1.1. Internal Sparse Field Test

This novel test method, designated the “internal sparse field” test, was developed by the STIS Instrument Definition Team. The method quantifies two key aspects of CTE effects on spectroscopic measurements: *(i)* The amount of charge lost *outside* a standard extraction

aperture, and (ii) the amount of centroid shift experienced by the charge that remains *within* that extraction aperture. This test utilizes the ability of the STIS CCD and its associated electronics to read out the image with any amplifier, i.e., by clocking the accumulated charge in either direction along both parallel and serial registers. A sequence of nominally identical exposures is taken, alternating the readout between amplifiers on opposite sides of the CCD (e.g., amps ‘B’ and ‘D’ for measuring parallel CTE performance). After correcting for (small) gain differences in the two readout amplifier chains, the observed ratio of the fluxes measured by the two amps can be fit to a simple CTE model of constant fractional charge loss per pixel transfer. Assigning  $ybin$  to be the CCD binning factor in the parallel clocking (“ $y$ ”) direction and  $y$  the pixel location of the target along the  $y$  axis where  $y = 1$  at the first pixel from the location of amp B<sup>1</sup>, the measured ratio of signals measured by amps B and D is

$$\frac{S_B}{S_D}(y) = \frac{CTE^{y*ybin}}{CTE^{1024-y*ybin}} = CTE^{2(y*ybin)-1024} \quad (1)$$

The dependence of the observed signal ratio (e.g.,  $S_B/S_D$ ) on the source position on the CCD confirms the consistency with a charge transfer effect (cf. Sections 2.2.1 and 3.1.1 below). The CTE is equal to the exponential of half the slope of  $\ln(S_B/S_D)$  vs.  $y$ .

A key virtue of this method is that it requires neither a correction for flat-field response, nor an a-priori knowledge of the source flux (as long as the input source is stable during the alternating exposures). It should be noted that what is being measured is a sum of the charge transfer inefficiencies for the two different clocking directions. However, for identical clocking voltages and waveforms and with the expected symmetry of the radiation damage effects, we believe the assumption that the CTE loss is equal in the two different clocking directions is a reasonable one.

The implementation of this “internal”<sup>2</sup> version of the sparse field test is as follows. Using an onboard tungsten lamp, the image of a long and narrow slit is projected at five positions along the CCD columns using special commanding of the STIS Mode Select Mechanism. At each position, a sequence of exposures is taken, alternating between the ‘B’ and ‘D’ amplifiers for readout. An illustration of such an exposure sequence is depicted in Figure 2. The exposure setup used for these observations is listed in Table 1, while the calibration program numbers and dates of each observing epoch are given in Table 2.

---

<sup>1</sup>This represents the nominal coordinate system of STIS CCD observations in the *HST* archive

<sup>2</sup>“internal” in this context means that all necessary observations use onboard lamps, so that such observations can be performed during Earth occultations, hence not requiring any valuable “external” *HST* observing time

The illumination of these images is representative for typical spectroscopic observations (as the dispersion direction of STIS CCD spectral modes is essentially along rows). The slit image has a narrow profile (2-pixel FWHM), similar to a point source spectrum. The CTE loss resulting from this test is “worst-case”, since there is hardly any background intensity (“sky”) to provide filling of charge traps in the CCD array.

After basic CCD reduction (subtraction of the bias overscan vector and bias image subtraction), the average flux per column within a 7-row extraction aperture [which is the default extraction size for 1-D spectral extractions in the CALSTIS pipeline used for STIS spectra of point sources, cf. Leitherer & Bohlin (1997); McGrath, Busko, & Hodge (1999)] as well as the centroid of the image profile within those 7 rows are calculated for each exposure. In order to reflect the flux measurement method used by the 1-D spectral extraction module of CALSTIS, a measurement of the background level is obtained 40 pixels above and below the extracted flux with a width of 5 rows. Flux and background measurements are performed using  $\kappa - \sigma$  clipping in order to reject cosmic rays and hot pixels. The alternating exposure sequence allows one to separate CTE effects from flux variations produced by warmup of the tungsten lamp. As the slit image extends across hundreds of columns, high statistical precision on CTE performance can be obtained even at low signal levels per column.

We emphasize that in calculating CTE loss from this test, charge is only considered “lost” if it is no longer within the standard 7-row extraction aperture. I.e., we are only measuring the component of CTE loss produced by relatively long-time-constant charge trapping. Hence, the CTI ( $= 1 - \text{CTE}$ ) values derived from this test will not agree with those measured by (e.g.) X-ray stimulation techniques using  $\text{Fe}^{55}$  or  $\text{Cd}^{109}$ , for which charge deferred to even the very first trailing pixel contributes to the CTI. However, the measurement described here *is* directly relevant to the estimation of CTE effects on STIS spectrophotometry.

### 2.1.2. Spectrophotometric Sensitivity Monitoring

Another set of data we use to characterize the CTE loss of the STIS CCD in spectroscopic mode is the calibration program that monitors the sensitivity of STIS spectroscopic modes. This program consists of wide-slit spectroscopy of primary and secondary spectrophotometric standard stars, using all supported STIS gratings. These data were taken on a regular basis, with a monitoring frequency depending on the grating (see Bohlin (1999) and Stys, Bohlin, & Goudfrooij (2004) for details). The particular value of this dataset in the context of characterizing the CTE loss is that the spectra of these stars (which are known to be intrinsically constant in time) provide a smoothly varying signal level along the dispersion direction, thus constraining the signal-level dependence of the CTE loss particularly well.

This is discussed further in Section 3.2.

## 2.2. Imaging Mode

### 2.2.1. External Sparse Field Test

Similar sparse-field CTE tests using “external” astronomical data have also been carried out in flight<sup>3</sup>. Series of imaging data were acquired on an annual basis for a field in the outskirts of the Galactic globular cluster NGC 6752, a field containing several hundreds of stars spanning a large range of intrinsic brightness. Every visit of the field consisted of 3 *HST* orbits, in which several exposures were taken using two different exposure times. Several repeat exposures were taken at both exposure times, alternating again between opposing readout amplifiers. Details of the imaging observations are listed in Table 3.

We deliberately chose a sparsely populated region in the outskirts of NGC 6752, as it is well known that the CTE-induced loss in crowded fields is significantly ameliorated (due to trap filling) relative to the effects on isolated point sources, while the latter is what we attempt to measure here. To allow an assessment of the effect of a varying sky background level, we took the data in the so-called Continuous Viewing Zone (CVZ) of *HST*, in which the bright Earth comes closer than usual to the telescope pointing direction. The varying amount of scattered light from the bright Earth allows one to obtain a varying “sky” background during the CVZ orbits, and hence to obtain measurements of CTI at a suitable range of sky background levels.

Basic CCD reduction steps were performed using tasks in the STSDAS.HST\_CALIB.STIS package of IRAF<sup>4</sup>. After performing bias and dark subtraction and flatfielding of each individual image using task BASIC2D, each set of images taken with a given exposure time is divided up in subgroups according to the sky background value of the individual images. The sky levels are derived by calculating the centroid of the histogram of sky pixel values windowed to  $\pm 4\sigma$  of the mean. This is done using an iterative procedure which rejects all pixels outside that window until the number of rejected pixels stays constant from one iteration to the next. Each subgroup is subsequently summed together (while performing cosmic-ray rejection; task OCRREJECT), and the summed image is divided by the number

---

<sup>3</sup>*HST* Program ID’s to date are 8415, 8854, 8911, and 9621.

<sup>4</sup>IRAF is distributed by the National Optical Astronomy Observatories, which is operated by the Association of Research in Astronomy, Inc., under cooperative agreement with the National Science Foundation, U.S.A.

of images combined. The sky background values of the resulting “final” images are listed in Table 3.

Aperture photometry is performed using the DAOPHOT-II package (Stetson 1987) as implemented within IRAF using fixed-size apertures. Three aperture sizes are used (radii of 2, 3, and 5 pixels) to evaluate the dependence of calculated CTI values on aperture size (see Section 3). An initial star coordinate list was established using the DAOFIND task, employing a detection threshold of  $5\sigma$  above the background. This initial list was then cleaned by eliminating targets close to bright stars, in order to avoid anomalous CTI measurements due to excessive filling of charge traps. Saturated stars were also eliminated. This cleaned coordinate list was used for all measurement epochs, using IRAF task XYXYMATCH to calculate the appropriate shifts and rotation angles to be applied to the reference coordinate list for each epoch.

Representative results on the parallel CTI for a short-exposure imaging dataset acquired in October 2001 are shown in Figure 3 in which the observed flux ratio (amp D/amp B) vs. CCD row number is plotted for four different ranges of stellar flux level per exposure. The expected CTE behavior is clearly seen, with the closer readout amplifier systematically measuring a higher stellar flux than the more distant amplifier. The drawn lines are fits of the CTE model we have been considering (i.e., Eq. 1) to the data. Note that the charge loss incurred for parallel clocking through the image area of the CCD can be quite substantial. For instance, panel (a) in Figure 3 shows that at that time, point sources with a detected signal of a few hundred electrons suffer from  $\sim 25\%$  charge loss when located 1000 rows away from the read-out amplifier. *Serial* CTI values were also determined (by reading out with amplifier ‘C’), and found to be negligible for all practical purposes (i.e., orders of magnitude smaller than the parallel CTI values, and consistent with zero within the uncertainties). The default gain = 1 setting (i.e.,  $1.0 e^-/\text{DN}$ ) is used throughout.

Best-fitting parallel CTI values for different sky background levels are plotted in Figure 4. This plot illustrates two obvious trends regarding the functional dependence of the CTE loss on source signal and background levels: (i) The CTI decreases with increasing source signal level, and (ii) At a given source signal level, the CTI decreases with increasing sky background levels. These dependencies are also seen in investigations regarding CTE loss of CCDs in the laboratory (e.g., Hardy, Murowinski, & Deen 1998).

A comparison of the fits to the data in the different panels of Figure 4 shows that the slope of  $\log(\text{CTI})$  vs.  $\log(\text{background})$  decreases systematically with increasing signal level. This suggests (i) that sky background fills traps in the *bottoms* of the potential wells of the CCD, thus mostly ameliorating the transfer of *small* charge packets, and (ii) a functional

dependence of the form

$$\text{CTI}(B, S) \propto \exp(-a(B/S)^b), \quad (2)$$

where  $B$  is the background level,  $S$  is the signal level, and  $a$  and  $b$  are free parameters. The substantial benefit of (only modest) sky background is good news for most science imaging observations with the STIS CCD, which typically have longer exposure times than those used for these tests and hence will not suffer from the large CTE effects experienced during the low-background tests reported here. The functional form of the dependence of CTI on signal and background levels will be discussed further in Section 3.

### 3. Results

This section is organized as follows. We first analyse the internal sparse field measurements to determine the time dependence of CTE loss and to illustrate CTE effects at low signal levels when used with the (supported but not commonly used) gain = 4 e<sup>-</sup>/DN setting. We then determine the functional forms to correct STIS CCD data for CTE loss as a function of observing mode (spectroscopy vs. imaging), signal level, and background level, and conclude with an examination of the dependency of the CTE loss on aperture size in imaging mode.

#### 3.1. Internal Sparse Field Data

##### 3.1.1. *The Time Dependence of CTE Loss and Centroid Shift*

The internal sparse field test was the only CTE test conducted with the STIS CCD in a uniform manner during both ground testing (at a signal level of  $\sim 3400$  e<sup>-</sup>, Malumuth 1996) and in-flight operation (on an annual basis). Due to the combination of this long baseline in time and the fact that CTI values measured from these data are of great precision (as hundreds of columns are averaged together during the analysis), we use these data to determine the time dependence of the CTE loss. On the other hand, these data are not used to derive the dependences of (spectroscopic) CTE loss on signal and background levels, given the fact that these data sample only one (low) background level per signal level, and this background level is different for the different signal levels.

A  $\chi^2$ -minimization algorithm is used to compute CTI values for each observing epoch and signal level. As outlined in Sect. 2.1.1, the observed ratio of the fluxes measured by the two amplifiers was fit to a simple CTE model of constant fractional charge loss per



pixel transfer, allowing for  $\kappa - \sigma$  clipping of outliers (the latter arise occasionally during the short (0.3 s) exposures due to lamp intensity fluctuations). Flux ratio results for the parallel internal sparse field test taken after 6.5 years in orbit are presented in Figure 5. As can be seen there, the simple CTE model fits the data well.

To derive the time dependence of the CTE loss, all measurements are first put on a uniform scale by normalizing them to one common background level  $B' = 0$ . To do so, two corrections are required: First, the effect of the spurious charge in STIS CCD bias frames (Goudfrooij & Walsh 1997; this is further discussed below) is accounted for by considering the total background ( $B'$ ) to be the measured one ( $B$ ) plus the spurious charge. Second, the background dependence of the CTI according to Eq. 7 (which is discussed in detail in Sect. 3.2) is taken into account. The time dependence is then derived by assuming a linear increase of CTI with time, as was found earlier for other CCDs aboard *HST* (e.g., Whitmore et al. 1999; Dolphin 2000), i.e., by fitting the zero-background CTI values to a function of the form:

$$\text{CTI}(t) = \text{CTI}_0 [1 + \alpha(t - t_0)], \quad (3)$$

with  $t$  in years and  $t_0 = 2000.6$ , the approximate midpoint in time of in-flight STIS observations. The conversion between  $(t - t_0)$  and the modified Julian date MJD (which is provided by keywords `TEXPSTRT` and `TEXPEND` in the science header of each STIS observation) is given by  $t - t_0 = (\text{MJD} - 51765)/365.25$ .

CTI values derived as mentioned above for the parallel internal sparse field test taken at different epochs are plotted in Figure 6. In-flight CTE degradation from a pre-flight starting point of low CTI is apparent. Typical CTE behavior is observed as a function of signal level: The *fractional* charge loss (which is proportional to CTI) drops with increasing signal level, while the *absolute* level of charge loss increases.

Results for the time-dependence fit for gain = 1 are shown in Figure 6 and Table 4. The functional fit to the data (shown as solid lines) is good, and the derived values for  $\alpha$  in Eq. 2 are consistent with one another (within the uncertainties) for all signal levels measured. After weighting the  $\alpha$  values of the individual fits by their inverse variance (i.e.,  $\text{RMS}^{-2}$ ), the weighted average time constant was found to be  $\alpha = 0.205 \pm 0.006$ , where the uncertainty represents the mean error of the mean.

The effects of charge trapping and release *within* the 7-row aperture are seen by examining the line profiles and centroids. Comparisons of the average line profiles seen for the opposing readout directions are shown in Figure 7 for two of the signal levels used. At 60 electrons per column, the charge trailing and centroid shift are obvious. Even at the higher

signal level, with much lower CTI, the magnified difference between the two observed profiles shows that the centroid shift is systematic and measurable. The measured centroid shifts (defined as half the difference between the profile centroids as measured by the B vs. the D amplifiers) after 5.5 years in orbit are plotted in the left panel of Figure 8, along with a least-square fit to the centroid shifts measured at the central position on the CCD as a function of measured gross signal level  $G$  as read out by the default amplifier D. The right panel of Figure 8 depicts the *evolution* of the centroid shift (at the central location on the CCD) due to CTE effects as a function of time. A comparison with Figure 6 shows that the centroid shifts increase in time with rates that are quite similar to those measured for the CTI values themselves.

All the above findings indicate that CTE effects cause a fractional loss of signal of which the amplitude is directly related to the size of the associated centroid shift, anywhere on the CCD. This is illustrated further in Figure 9, which reveals an extremely tight relation between measured CTI and centroid shift. The solid line depicts the least-square fit to this relation,

$$\text{Centroid Shift [pixels]} = 0.081 \left( \frac{\text{CTI}}{10^{-4}} \right) - 0.002 \left( \frac{\text{CTI}}{10^{-4}} \right)^2 \quad (4)$$

which has an RMS error of only 0.01 pixels. (Note that positive centroid shifts in this equation indicate shifts toward *smaller* Y coordinate values in the nominal STIS coordinate system.) This relation should prove useful to spectroscopic programs for which both accurate flux calibration *and* astrometry is important.

Similar measurements have also been carried out in the serial clocking direction by projecting vertical slit images at several positions along the CCD rows and alternating between amplifiers ‘C’ and ‘D’ (cf. Figure 1) for readout. The resulting charge loss is *much* smaller than for the parallel case and stays below 1% for 1024 pixel transfers, even for the lowest signal level measured. This significant difference between the CTE loss experienced in the two clocking directions is mainly due to the difference in clocking time, which is a factor  $\sim 30$  faster in the serial direction for the STIS CCD ( $22 \mu\text{s pixel}^{-1}$  in serial vs.  $640 \mu\text{s pixel}^{-1}$  in the parallel direction; see also Bristow & Alexov 2002). Centroid shifts in the serial clocking direction are also very small but still well determined, due to the statistical precision offered by averaging over hundreds of rows. Interestingly, the serial CTI values and centroid shifts are consistent with the relation found above in Eq. 4. This is illustrated in Figure 10. Given the negligible CTE loss experienced by the STIS CCD in the serial clocking direction, the remainder of this paper only addresses the *parallel* CTE loss.

### 3.1.2. CTE Effects at Low Signal Level: Issues for the Gain = 4 Setting

As mentioned above in Section 2.2.1 and shown in Figure 4, there is a strong dependence of the CTE loss on background level, especially for low signal levels. In fact, this effect is significant enough for the structure of STIS CCD bias frames to cause an apparent non-linearity in the CTI values derived from the internal sparse field tests at the lowest signal levels. This is illustrated in Figure 11. The data are shown in two panels per signal level, one for each supported CCD gain setting (1.00 and 4.08 e<sup>-</sup>/DN, hereafter referred to as gain = 1 and gain = 4 respectively). The open symbols depict actual flux measurements (flux levels are indicated on the left ordinate) of the epoch 2002 data of the internal sparse field test. The flux measurements with the B and D amps were averaged together for this purpose, after having flipped the CCD row numbers for the B-amp measurements around the central row (#512) in order to coincide with the D-amp rows. The error bars indicate the measurement repeatability. The gain = 4 setting features a CTE-induced loss that is significantly smaller than that for the gain = 1 setting. The dashed lines depict the structure of STIS bias frames (after subtraction of the overscan vector) in the appropriate gain setting along CCD columns. The STIS CCD suffers from accumulative *spurious charge*, which causes a row-dependent amount of extra “background” that is added during readout (see Goudfrooij & Walsh 1997). The amount of added spurious charge for the gain = 4 setting is much larger than that for gain = 1 (due to a difference in parallel clocking voltages employed), and the slope in the spurious charge level across the lower half of the CCD is much steeper for gain = 4 than for gain = 1 bias frames. This is the main cause of the difference in low-signal level CTE behavior between the two gain settings. Jumping ahead, the filled symbols in Figure 11 depict the result of the application of the CTE correction formula (Eq. 7) derived in Section 3.2 below. The corrected fluxes are uniform across the CCD to within  $\sim 1 \sigma$  for gain = 1, while gain = 4 data at low signal levels are still somewhat affected by the slope of the spurious charge in the bias frames. Hence, the accuracy of the CTE corrections discussed below formally applies only to gain = 1 data (and gain = 4 data at signal levels  $\gtrsim 2000 \text{ e}^-$ )<sup>5</sup>.

---

<sup>5</sup>The main purpose of the gain = 4 setting of the STIS CCD is to enable very high signal-to-noise observations, using signal levels up to the intrinsic full well of the CCD, at the cost of a higher read noise than for gain = 1 (see Chapter 7 in Kim Quijano et al. 2004). This behavior at low signal levels is therefore not detrimental for *typical* data taken in gain = 4.

### 3.2. Functional Forms for CTE Corrections

Since spectroscopy and imaging involve inherently different detector illumination patterns, CTE measurements are expected to show different dependencies on signal level and background level for the two observing modes. For instance, a given total signal level within a certain aperture size in imaging mode contains a substantial range of signal levels *per CCD column*, and the charge in each of those CCD columns suffers from a different percentage of CTE loss. With this in mind, we chose to determine functional forms to characterize the CTE loss of the STIS CCD separately for spectroscopy and imaging modes.

#### 3.2.1. Spectroscopy Mode

**Dependence on Signal and Background Level** To constrain the dependence of spectroscopic CTE loss on signal and background levels, we utilize a variety of spectra of spectrophotometric standard stars taken during the last few years of STIS operations, when CTE effects were most significant. The standard star spectra used to characterize the CTE effects in this report are listed in Table 5 along with their measured signal and background levels. All spectra used a 2'' wide slit to render slit losses negligible. Spectra are calibrated using CALSTIS *without* applying any CTE correction, and extracted using traces measured from the spectra themselves (see Dressel et al. (2006) regarding the evolution of spectral traces with STIS). CTI values for spectra of DA white dwarf flux standards GD 71 and LDS 749B taken using the G230LB grating are derived from the ratio of their measured fluxes by those measured from G230L spectra. The (time-dependent) sensitivity calibration for the G230L mode (which uses the NUV-MAMA detector of STIS (a microchannel-plate based photon-counter, not a CCD) and hence does *not* suffer from CTE loss) is very well established and accurate to subpercent level (Stys et al. 2004), while the sensitivity calibration for the CCD spectral modes was established from flux standard star spectra with signal levels high enough ( $\gtrsim 2 \times 10^4$  e<sup>-</sup>/extraction) to render CTE effects negligible. Figure 12 shows the CTI values obtained this way from the G230LB spectra of flux standard stars GD 71 and G191–B2B listed in Table 5, which share a common background level. Prior to plotting, these CTI values were first normalized to epoch 2000.6 (see Sect. 3.1.1 above). The charge loss for low-signal spectra is already quite significant in mid-2000, rising above 10% below an extracted signal level of  $\sim 200$  e<sup>-</sup> for spectra taken at the nominal central position on the CCD. Figure 12 shows that the logarithm of CTI scales roughly linearly with the logarithm of signal level, i.e.:

$$\text{CTI}(G) \propto \alpha G^{-\beta}, \tag{5}$$

where  $G$  is the (gross) signal level and  $\alpha$  and  $\beta$  are free parameters. For the G430L and G750L spectra in Table 5, CTI values are derived by comparing the observed fluxes with pure hydrogen white dwarf models, as detailed in Bohlin, Collins, & Gonnella (1997). The range of extracted signal levels covered by the spectra used here is  $\sim 20 - 16,000 \text{ e}^- \text{ pixel}^{-1}$ , which should encompass all spectroscopic observations for which CTE loss is an issue. Smoothed versions of the spectra are shown in panel (a) of Figure 13.

For the expected basic functional form of the dependence of the CTE loss on signal and background levels we combine Eqs. 2 and 5:

$$\text{CTI}(B, G) = \alpha G^{-\beta} \exp(-\gamma (B'/G)^\delta), \quad (6)$$

where  $B'$  is the *total* background signal level (i.e., the sum of the sky background  $B$ , the dark current, and the spurious charge in STIS bias frames which is  $0.5 \text{ e}^- \text{ pixel}^{-1}$  for gain = 1 and  $5.0 \text{ e}^- \text{ pixel}^{-1}$  for gain = 4),  $G$  is the gross signal level, and  $\alpha$ ,  $\beta$ ,  $\gamma$  and  $\delta$  are free parameters. The values for  $B$  and  $G$  are readily obtained from the output of the x1D routine within CALSTIS to extract 1-D spectra (McGrath et al. 1999). The background spectrum in x1D is smoothed in the spatial and dispersion directions prior to subtraction; this smoothed version is the  $B$  used in Eq. 6.

An attempt to fit the function in Eq. 6 to the CTI values measured for the spectra in Table 5 showed that the CTI values of the G230LB and G430L spectra can be fit very well this way. However, the CTI values measured for the red end of the wavelength coverage of the G750L spectra are systematically found to be below the predictions of this fit. This is illustrated in panels (b) and (c) of Figure 13 which show the best fit of Eq. 6 to the G230LB and G430L data and the residual percentage of flux error after correcting the data for the CTE loss associated with that fit, respectively. In the following we attempt to correct for this problem by parametrizing the background parameter in Eq. 6 in terms of the influence of the signal in the wings of the point-spread function (PSF) to the filling of charge traps during the CCD readout procedure.

**The Impact of the “Red Halo” of the PSF of the STIS CCD** The PSF of the STIS CCD features broad wings at wavelengths  $\gtrsim 8000 \text{ \AA}$  (e.g., Leitherer & Bohlin 1997), the width of which increases strongly with increasing wavelength. This “red halo” is believed to be due to scatter within the CCD mounting substrate which becomes more pronounced as the silicon transparency increases at long wavelengths. The effects of the red halo are significant, particularly redward of  $9500 \text{ \AA}$  where the default 7-pixel extraction box captures only  $\lesssim 70\%$  of the light in the PSF (Leitherer & Bohlin 1997).

This extended halo is likely to have a significant effect on the CTE loss experienced by

the signal within the default 7-pixel extraction box, since the charge induced by the halo signal that is clocked out *before* the signal of the source spectrum (i.e., the halo signal on the side of the read-out amplifier) should act effectively as ‘background’ in filling charge traps. Note that the red halo signal is not included in the background term  $B'$  in Eq. 6, since the background spectrum used within CALSTIS/X1D is measured far away from the spectrum location<sup>6</sup>. To improve this situation, we separate the background term into two distinct terms,  $B'$  (as before) and a new term  $H$  which contains the fraction of PSF signal between the default 7-pixel extraction box and the read-out amplifier. Values for  $H$  as a function of wavelength are derived from existing CALSTIS reference files (namely from the Photometric Correction Tables<sup>7</sup>). We plot these  $H$  values in Figure 14. While  $H$  is non-negligible at any wavelength, the spatial extent of the PSF beyond the default extraction box is only a few CCD pixels below  $\sim 8000 \text{ \AA}$ . Hence, low values of  $H$  do *not* necessarily lower the CTE loss significantly. This issue is accounted for in two ways: (i) by subtracting a certain minimum threshold value from the measured value of  $H$  (i.e., parameter  $\eta$  in Eq. 7 below), and (ii) by neglecting the halo term for gratings other than G750L or G750M.

Taking all of the above into account, the full functional form of the CTI algorithm considered for spectroscopic modes is

$$\text{CTI}_{SP} = \alpha G^{-\beta} (\gamma(t - 2000.6) + 1) \exp\left(-\delta \left[\frac{B' + \epsilon H'}{G}\right]^\zeta\right) \quad (7)$$

where  $H' = \max(0.0, (H - \eta)) \times \text{Net}$ .

( $\text{Net} = G - 7B$ , the net counts in the extracted spectrum.) Initial estimates of the values of parameters  $\alpha$  through  $\eta$  and their uncertainties were made using bootstrap tests (except for the CTI time constant  $\gamma$ , which was fixed at 0.205 as discussed in Sect. 3.1.1 above). Particular attention was given to achieving a suitable fit for the full range of signal and background levels sampled. A robust fit parameter was then minimized using a non-linear minimization routine from *Numerical Recipes* (Press et al. 1992). Best-fit values of the parameters  $\alpha$  through  $\eta$  are listed in Table 6.

The quality of this parametrization of the spectroscopic CTE loss is illustrated in Figures 6 and 13. The dotted lines in the left panel of Figure 6 show the CTI values predicted by Eq. 7 for the internal sparse field data at the different gross signal levels (and  $B' = 0$ ). It can be seen that Eq. 7 fits those data within the uncertainties<sup>8</sup>. Figure 13 shows the fit of

---

<sup>6</sup>300 unbinned CCD pixels away by default.

<sup>7</sup>\*\_pct.fits, listed in data header keyword PCTAB.

<sup>8</sup>The small offset for the 60 e<sup>-</sup>/extraction data is due to the effect of the small slope of the spurious charge

Eq. 7 to the standard star spectra, both with and without the  $H$  term mentioned above. A comparison of panels (c) and (e) of Figure 13 in particular clarifies that the inclusion of the  $H$  term yields a significantly better correction for the red end of G750L spectra. Overall, the new parametrization of the CTE loss is accurate within 5% for any data point in the spectra used here, while the RMS accuracy for all spectra used in this study together stays within 1%. For reference, the dotted lines in panel (e) in Figure 13 depict the Poisson noise associated with a resolution element (assumed to be 2 pixels along the dispersion) in spectra of a given signal level. *This CTE correction formula renders spectroscopic flux calibration to an accuracy better than the uncertainty due to Poisson noise per resolution element.*

### 3.2.2. Imaging Mode

CTI values are calculated for every epoch of the external sparse field test as explained in Sect. 2.2.1, grouped by ranges of flux and sky background levels. The ranges of signal levels are chosen after inspecting histograms of signal levels for each sky level listed in Table 3, aiming for similar numbers of targets in each group. Table 7 lists the derived CTI values for each group and epoch.

**Time Dependence: Consistency With Spectroscopic Mode** Before embarking on a comprehensive procedure to fit the imaging CTI values as a function of signal and background levels, we derive the time dependence of the CTE loss from these data and check for consistency with the time constant derived before in Sect. 3.1.1 for spectroscopic mode. To this end, we select groups of signal and sky levels that were measured consistently in at least three epochs and whose CTI uncertainties were smaller than the CTI values themselves. The CTI values of these groups are plotted in Figure 15 as a function of time, along with least-squares fits of CTI vs. time (separately to each group). After weighting the slopes of the individual fits by their inverse variances, the weighted average time constant is  $0.214 \pm 0.047$ , i.e., consistent with the  $0.205 \pm 0.006$  found in Sect. 3.1.1. We adopt the latter in the following, given the much longer time baseline and the more homogeneous and well-determined data used to derive it.

**Dependence on Signal and Background Level** The functional form to characterize the CTI of the STIS CCD in imaging mode was determined in a way similar to that of the

---

level in the lower half of STIS CCD bias frames, as discussed in Sect. 3.1.2 and illustrated in Figure 11.

spectroscopic mode. We first attempted to fit the imaging CTI values with the function in Eq. 6 used to fit the spectroscopic CTI values, but found that the dependence on background level required more terms in this case. After extensive experimentation, the following functional form produced the best fit to the imaging data:

$$\text{CTI}_{IM} = a e^{-b \text{ lcts}} \times (c(t - t_0) + 1) \times \left[ d \exp(-e \text{ lbck}) + (1 - d) \exp\left(-f \left(\frac{\text{bck}}{\text{counts}}\right)^g\right) \right] \quad (8)$$

where ‘counts’ stands for the net counts within the measurement aperture, and

$$\begin{aligned} t - t_0 &\equiv (\text{MJD} - 51765)/365.25 \\ \text{lcts} &\equiv \ln(\text{counts}) - 8.5 \\ \text{bck} &\equiv \max(0.0, \text{sky}) \\ \text{lbck} &\equiv \ln(\text{sqrt}(\text{bck}^2 + 1)) - 2 \end{aligned}$$

The constants 51765, 8.5, and 2 were roughly the averages of the corresponding parameters in the data, and were included to provide numerical stability as well as to produce independent coefficients ( $a$  through  $g$ ). The purpose of the ‘bck’ and ‘lbck’ parameters is to avoid logarithms of negative values. (The parameter  $c$  was fixed to 0.205 as discussed above.) The fitting procedure was the same as that used in Sect. 3.2.1 above. The resulting best-fit values of the coefficients in Eq. 8 are listed in Table 8.

The quality of this parametrization of the CTE correction is depicted in Figure 16. Quantitatively, it yields a correction that is accurate within  $4\sigma$  of *any* single data point in Table 7, while the overall RMS uncertainty is 3.0%, which is equivalent to  $0.2\sigma$  of the “mean” data points plotted in panel (b) of Figure 16. To put this in perspective, an observation of a typical faint star in September 2002 with an extracted signal of  $100 e^-$  and a background of  $6 e^-$  per pixel at the center of the CCD underwent a CTE loss of  $\sim 15\%$  (cf. Figure 15). The parametrization in Eq. 8 corrects this loss to an RMS photometric accuracy of only 0.5%, *much lower than that due to Poisson noise for that object.*

**Centroid Shifts in Imaging Mode** Centroid shifts were also measured for the external sparse field imaging data, defined (as before) as half the difference between the centroids of the target stars as measured by the two different amplifiers.

The derived centroid shifts are plotted against measured CTI in Figure 17, which shows a strong relation between the two parameters, similar to the case for the spectroscopic data described in Sect. 3.1.1. The solid line depicts a weighted least-square fit to this relation for the imaging data,

$$\text{Centroid Shift [pixels]} = 0.025 \left(\frac{\text{CTI}}{10^{-4}}\right) - 0.78 \cdot 10^{-3} \left(\frac{\text{CTI}}{10^{-4}}\right)^2 \quad (9)$$



which has an RMS error of 0.005 pixels<sup>9</sup>. We emphasize that centroid shifts due to CTE effects are rarely taken into account (a literature search using the NASA Astrophysics Data System<sup>10</sup> came up with only one study: Piatek et al. 2005), whereas they are relevant for science programs that aim to reach the highest possible positional accuracy such as proper motion measurements for which accuracy of order 0.01 pixel is often required (e.g., McNamara, Harrison, & Anderson 2003; Koslowski et al. 2006). This is especially important if one combines measurements done with two different instruments (or with one instrument but at significantly different locations on the CCD) to derive proper motions.

A comparison of Eq. 9 with Eq. 4 (or, equivalently, Figure 17 with Figure 9) shows that the imaging data incur a roughly 3 times smaller centroid shift than spectroscopic data for a given CTI value. We interpret this difference in the sense that the measured centroid shifts are most heavily influenced by the centroid shift incurred by the *peak pixel* of the PSF (since it is by far the brightest pixel within the measurement aperture), and higher signal levels cause lower centroid shifts. To give an illustrative estimate of this effect: A comparison of Eq. 8 with Eq. 7 shows that for a given CTI value and background level, the signal level in imaging mode is a factor  $\sim 7$  higher than in spectroscopic mode. Approximating the imaging and spectroscopic PSFs by Gaussians with a FWHM of 1.8 pixels, this translates to a ratio in peak intensity

$$\frac{Peak_{IMA}}{Peak_{SPEC}} = \frac{7}{\sqrt{\pi/(4 \ln 2)} \text{FWHM}_{\text{PSF}}} \sim 3.6.$$

According to Eq. 7, a 3.6 times higher signal level causes a  $\sim 3.0$  times lower CTI value, and hence a 2.9 times lower centroid shift (cf. Eq. 4), which is consistent with what we find in practice.

**The Effect of Aperture Size for Imaging Mode** Since the amplitude of the centroid shift increases with CTE loss as discussed above, one obvious question is whether this effect has an impact on small-aperture photometry, which is often used in imaging programs of compact sources in order to achieve an increased signal-to-noise ratio relative to the use of larger apertures. We checked for this by evaluating the dependence of the measured CTE loss on aperture size using the imaging data of the external sparse field test. Photometry measurements were made through three aperture sizes (radii of 2, 3, and 5 pixels). The result is illustrated in Figure 18. There is no significant difference in CTI value among the three apertures used: The formal ratio between CTI values measured through 3-pixel radius

---

<sup>9</sup>Again, positive centroid shifts in this equation indicate shifts toward *smaller* Y coordinate values.

<sup>10</sup><http://www.adsabs.harvard.edu>

and through 2-pixel radius apertures for the data shown in Figure 18 is  $0.998 \pm 0.015$  (mean error of the mean). Likewise, the ratio between CTI values measured through 5-pixel radius and through 2-pixel radius apertures is  $1.031 \pm 0.020$ . We interpret this result in the sense that the centroid shift to the PSF caused by CTE effects does not cause actual loss of signal as long as one measures the centroids of the targets on the image itself with an adequately large centering box width<sup>11</sup>.

### 3.3. Implementation of CTE Correction

As we have adopted the definition of CTE as the fraction of charge transferred per pixel transfer, the correction for CTI ( $\equiv 1 - \text{CTE}$ ) to be applied to an extracted STIS data point *OBJ* (be it a flux element of a STIS CCD spectrum<sup>12</sup> or an entry of a star in a photometry table from STIS CCD imaging) is

$$OBJ_{CORR} = \frac{OBJ}{(1 - CTI_{OBJ})^{1024 - y * ybin}} \quad (10)$$

where  $y$  is the Y coordinate of the centroid of the target,  $ybin$  is the on-chip binning factor, and  $CTI_{OBJ}$  is the result of Eq. 7 [for spectroscopic data] or Eq. 8 [for imaging data] for that data point.

## 4. Concluding Remarks

Using a variety of methods, a set of formulae to correct observations of point sources with the STIS CCD for CTE-related loss of signal has been derived and presented. For data taken in imaging mode, the CTE loss is parametrized in terms of the location of the source on the CCD, the source signal level within the measurement aperture, the background level, and the time of observation. For spectroscopic data, one extra parameter is needed to provide an adequate calibration of the CTE loss, namely the signal in the point spread function located between the signal extraction box and the read-out amplifier. The effect of the latter parameter is significant at wavelengths redward of 8000 Å where the PSF of the STIS CCD exhibits an extended “halo”, i.e., for spectra taken using the G750L or G750M gratings of STIS. The algorithms presented here correct flux calibration inaccuracies due to

---

<sup>11</sup>We used the default size of the centering box within DAOPHOT-II (CBOX = 5 pixels).

<sup>12</sup>Note however that since December 16, 2003, the pipeline flux calibration of STIS CCD spectra takes correction for CTI already into account for full-frame datasets (Goudfrooij & Bohlin 2006).

CTE losses as large as 30% to within  $\sim 1.5\%$  RMS throughout the wavelength range covered by the STIS CCD observing modes.

Using bi-directional CCD readouts, centroid shifts incurred due to CTE loss are also derived. Centroid shifts are up to  $\sim 10^{-1}$  pixel for imaging photometry of faint point sources, and a factor of  $\sim 3$  higher for spectroscopy mode. A strong correlation is found between the signal loss and the centroid shift (both for imaging and spectroscopic modes), thus enabling one to correct for both effects of imperfect CTE to STIS CCD observations. While centroid shifts due to CTE effects are rarely taken into account in the literature, they are relevant for science programs that aim to reach the highest possible positional accuracy such as proper motion measurements for which accuracy of order 0.01 pixel is often required.

Though we have demonstrated that the correction formulae work well, it is of course preferable (when practical) to minimize the magnitude of the CTE effects on an observing program at the data acquisition stage. To this end, STIS operations support acquisition of targets for CCD spectroscopic modes at the so-called ‘E1 pseudo-apertures’, which are located  $\sim 125$  rows from the readout amplifier rather than at field center. The appropriate instrumental calibrations have been developed for these aperture positions. At the STIS plate scale of 0.05 arcseconds per pixel along the slit, this position gives 6 arcseconds of sky coverage to the near edge of the CCD; targets for which this angular coverage is sufficient can thus be observed with four times lower charge loss by selecting this observing position rather than the center of the CCD. Corrections for CTE loss and the use of the ‘E1 pseudo-apertures’ will be of even greater importance in the future if STIS is successfully repaired as planned in the hoped-for HST Servicing Mission 4, as the CCD usage will be extended for a number of additional years in the orbital radiation environment.

**Acknowledgments** We are grateful to the anonymous referee for a quick and thorough review, and for making constructive suggestions that improved the paper. We acknowledge the valuable contributions of Tom Brown, Ron Gilliland, and Mike Potter to STIS CTE analysis in the past.

## REFERENCES

- Bohlin, R. C., 1999, Instrument Science Report STIS 1999-07 (Baltimore: STScI)
- Bohlin, R. C., Collins, N., & Gonnella, A., 1997, Instrument Science Report STIS 1997-14 (Baltimore: STScI)

- Bohlin, R. C., & Goudfrooij, P., 2003, Instrument Science Report STIS 2003-03R (Baltimore: STScI)
- Bristow, P., & Alexov, A., 2002, ST-ECF Instrument Science Report CE-STIS 2002-001 (Garching: ST-ECF)
- Dolphin, A. E., 2000, PASP, 112, 1397
- Dressel, L. L., Barrett, P. E., Goudfrooij, P., & Hodge, P. E., 2006, in Proc. 2005 HST Calibration Workshop, eds. A. M. Koekemoer, P. Goudfrooij, & L. L. Dressel (Baltimore: STScI), 267
- Gilliland, R. L., Goudfrooij, P., & Kimble, R. A., 1999, PASP, 111, 1009
- Goudfrooij, P., & Walsh, J. R., 1997, Instrument Science Report STIS 1997-09 (Baltimore: STScI)
- Goudfrooij, P., & Kimble, R. A., 2003, in 2002 HST Calibration Workshop, eds. S. Arribas, A. Koekemoer, & B. C. Whitmore (Baltimore: STScI), p. 105
- Goudfrooij, P., & Bohlin, R. C., 2006, Instrument Science Report STIS 2006-03 (Baltimore: STScI)
- Hardy, T., Murowinski, R., & Deen, M. J., 1998, IEEE Trans. Nucl. Sci., 45, 154
- Janesick, J., Soli, G., Elliot, T., & Collins, S., 1991, SPIE Electronic Imaging and Technology Conference on “Solid State Optical Sensors II,” 1147
- Kimble, R. A., Brown, L., Fowler, W. B., Woodgate, B. E., Yagelowich, J. J., et al., 1994, Proc. SPIE, 2282, p. 169
- Kimble, R. A., Goudfrooij, P., & Gilliland, R. L., 2000, Proc. SPIE, 4013, p. 532
- Kim Quijano, J., et al., 2004, STIS Instrument Handbook (Baltimore: STScI)
- Koslowski, S., Woźniak, P. R., Mao, S., Smith, M. C., Sumi, T., Vestrand, W. T., & Wyrzykowski, L., 2006, MNRAS, doi:10.1111/j,1365-2966.2006.10487.x
- Leitherer, C., & Bohlin, R. C., 1997, Instrument Science Report STIS 97-13 (Baltimore: STScI)
- Malumuth, E. M., 1996, Pre-launch STIS Analysis Report #55 (Greenbelt: NASA/GSFC)
- McGrath, M. A., Busko, I., & Hodge, P., 1999, Instrument Science Report STIS 99-03 (Baltimore: STScI)

- McNamara, B. J., Harrison, T. E., & Anderson, J., 2003, *ApJ*, 595, 187
- Piatek, S., Carlton, P., Bristow, P., Olszewski, E. W., Harris, H. C., Mateo, M., Minniti, D., & Tinney, C. G., 2005, *AJ*, 130, 95
- Proffitt, C. R., 2006, in *Proc. 2005 HST Calibration Workshop*, eds. A. M. Koekemoer, P. Goudfrooij, & L. L. Dressel (Baltimore: STScI), 199
- Riess, A., & Mack, J., 2004, *Instrument Science Report ACS 2004-06* (Baltimore: STScI)
- Stetson, P. B., 1987, *PASP*, 99, 191
- Stys, D. J., Bohlin, R. C., & Goudfrooij, P., 2004, *Instrument Science Report STIS 2004-04* (Baltimore: STScI)
- Whitmore, B. C., Heyer, I., & Casertano, S., 1999, *PASP*, 111, 1559
- Woodgate, B. E., Kimble, R. A., Bowers, C. W., Kraemer, S., Kaiser, M. E., et al., 1998, *PASP*, 110, 1183

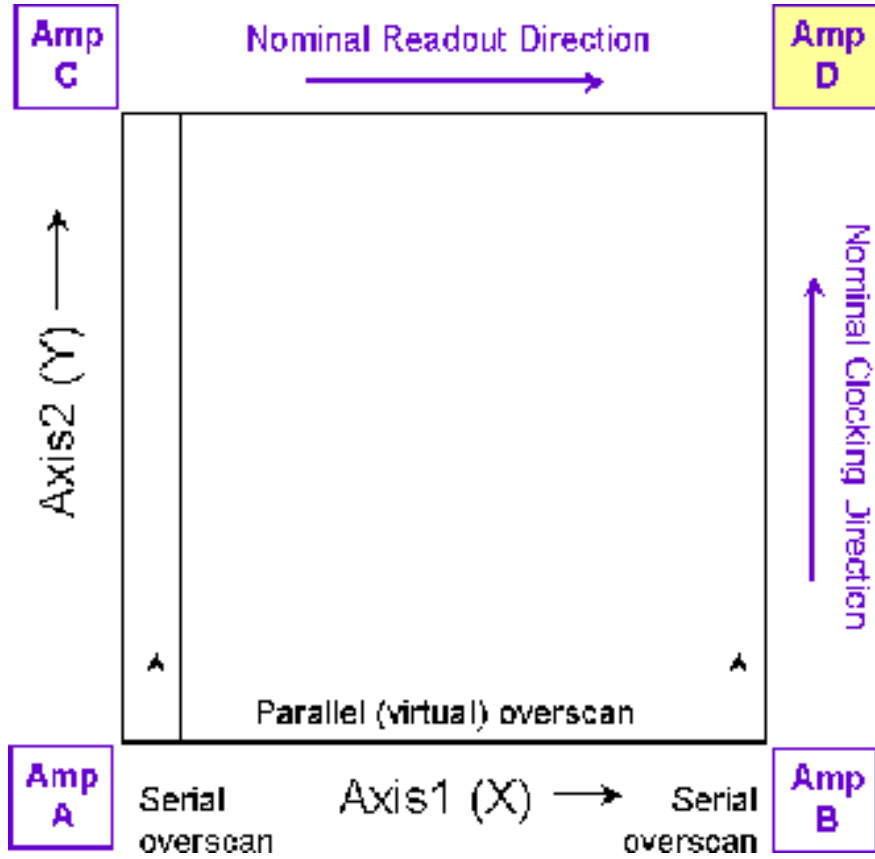


Fig. 1.— Schematic architecture of the STIS CCD. The  $1024 \times 1024$  pixel device has two serial registers and four readout amplifiers. The image can be read out through any single amplifier or via two- and four-amplifier combinations. The nominal amplifier (amp D) is at the top right.

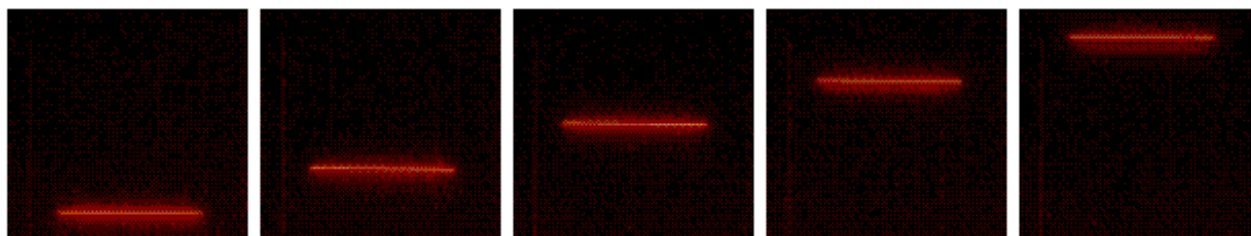


Fig. 2.— Representative images used for the “internal” sparse field CTE test in the parallel clocking direction. At each of the five positions along the CCD columns, a sequence of exposures is taken, alternating between amplifiers ‘B’ and ‘D’ (see Figure 1). Systematic variation of the relative signals measured by the two amplifiers as a function of position reveals the CTE effects. The images are displayed at a logarithmic stretch.

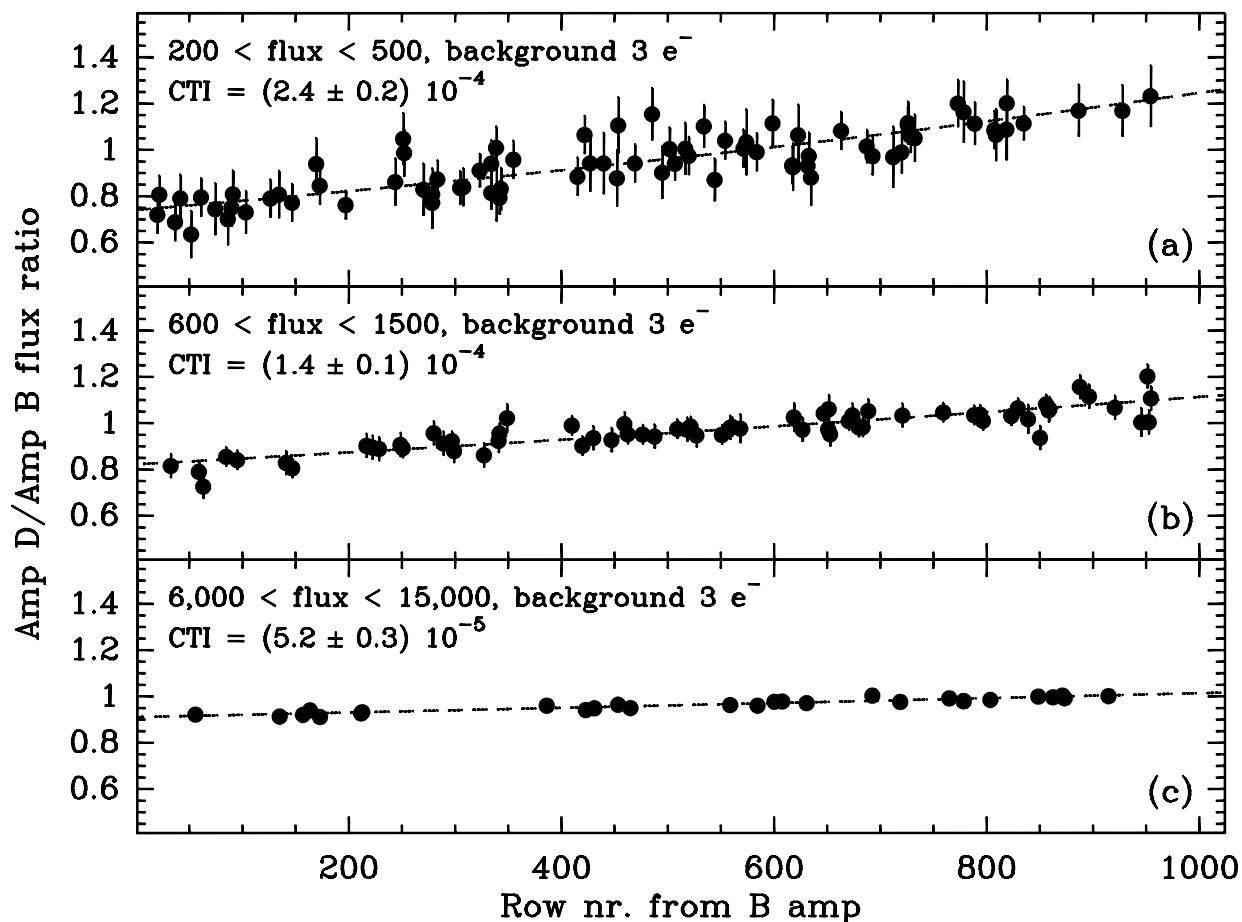


Fig. 3.— Flux ratio results for the external imaging sparse field CTE test in the parallel clocking direction, taken in October 2001 (after 4.7 years in orbit). The sky background was  $3 e^-/\text{pixel}$ . The three panels correspond to measurements at different signal levels, as shown in the legends. In each panel, the ratio of the signals measured by the two different amplifiers is plotted as a function of the Y position of the image along the CCD columns. The best-fitting simple CTE model (constant fractional charge loss per pixel transfer) as well as the corresponding CTE value are shown in each panel. The stellar fluxes shown here were measured using a circular aperture with a radius of 3 pixels.



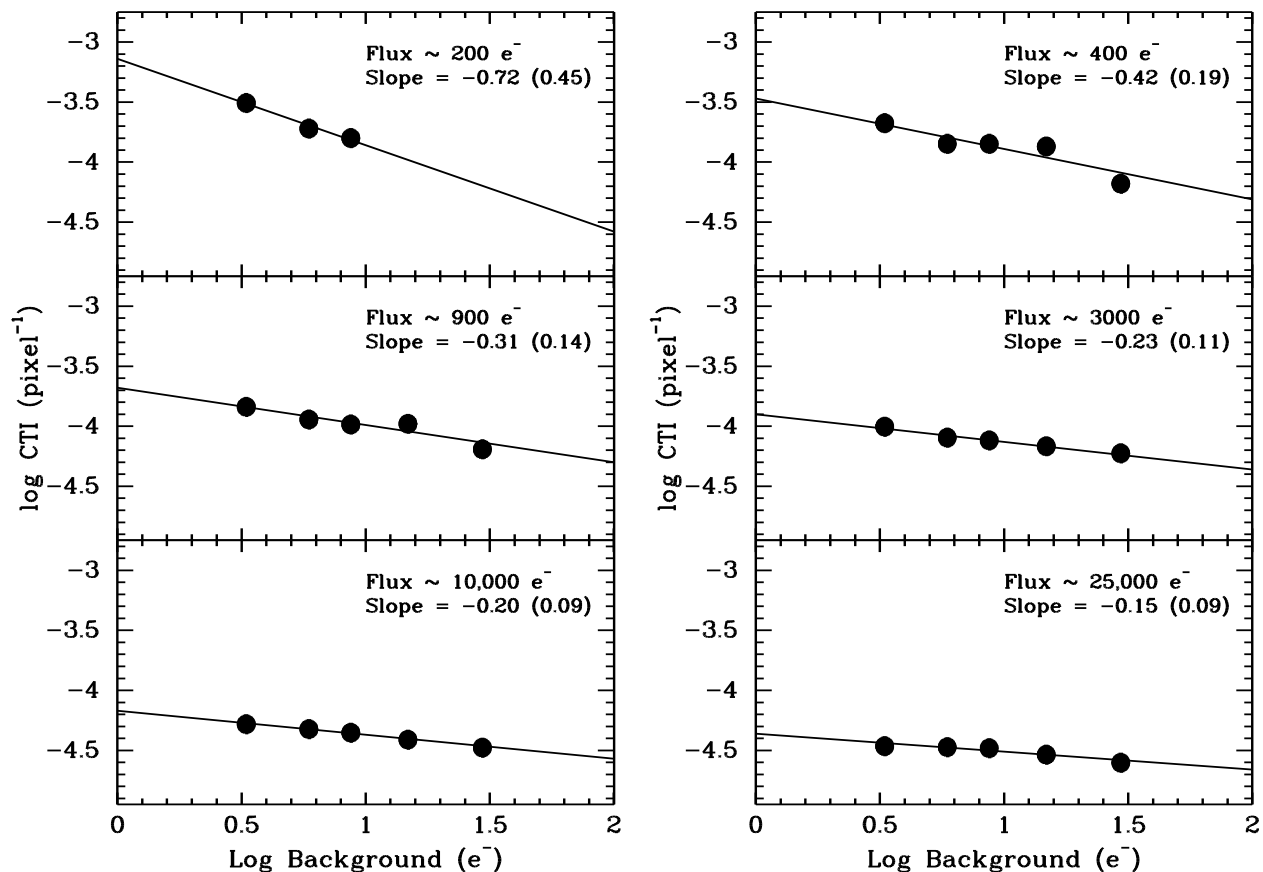


Fig. 4.— Log-log plot of CTI vs. sky background level for six different signal levels, derived from the external imaging sparse field test taken after 4.7 years in orbit. The flux levels, the slopes of the best-fitting line, and the latter’s uncertainties (in parentheses) are mentioned in each panel. Note the systematic decrease of the CTI dependence on the sky background with increasing signal level.

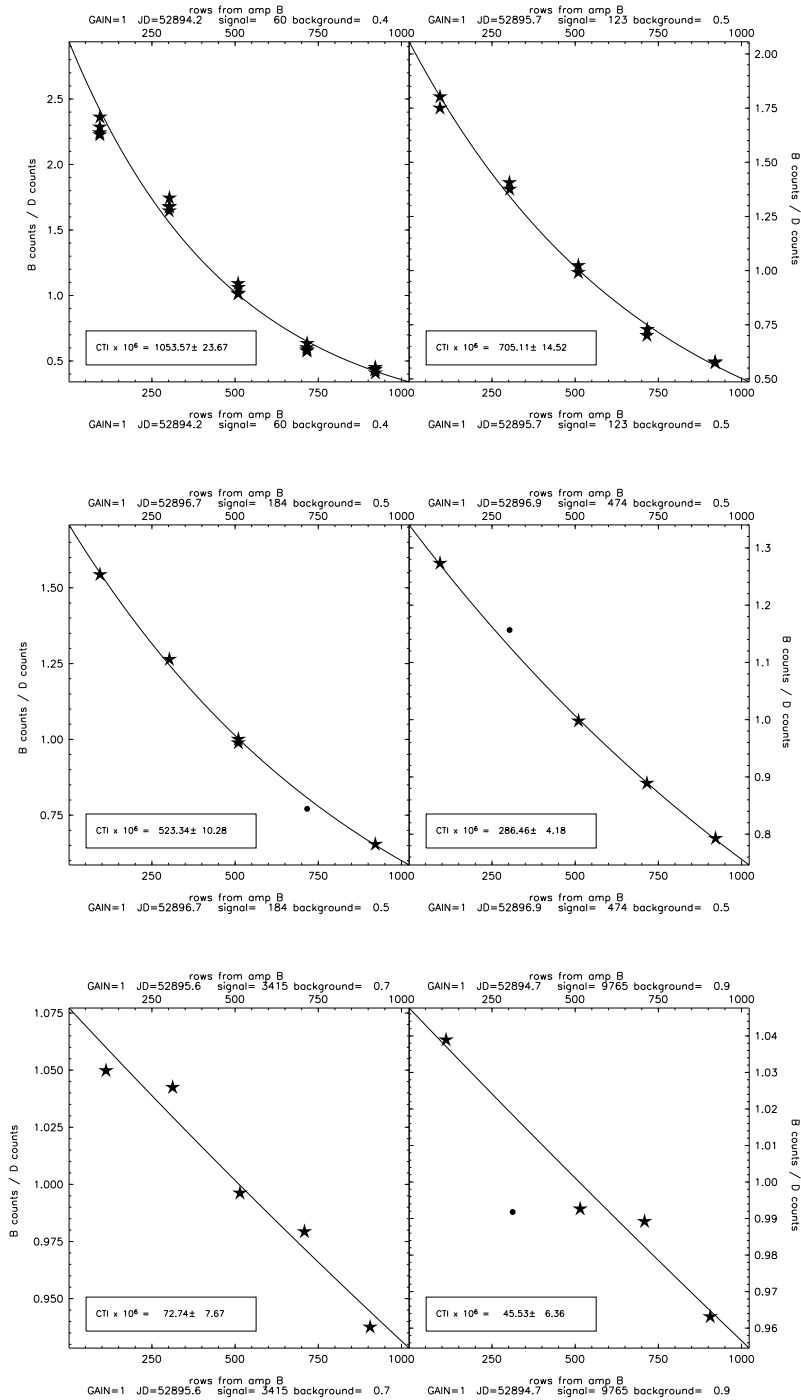


Fig. 5.— Flux ratio results for the 2002 epoch of the internal sparse field CTE test in the parallel clocking direction. The six panels correspond to measurements at different signal levels, as indicated above and below each panel. In each panel, the ratio of the signals measured by the two different amplifiers is plotted as a function of the mean Y position of the image along the CCD columns. The best-fitting simple CTE model (constant fractional charge loss per pixel transfer) as well as the corresponding CTI value are shown in each panel. Star symbols indicate measurements used in the fit and circles indicate rejected points.

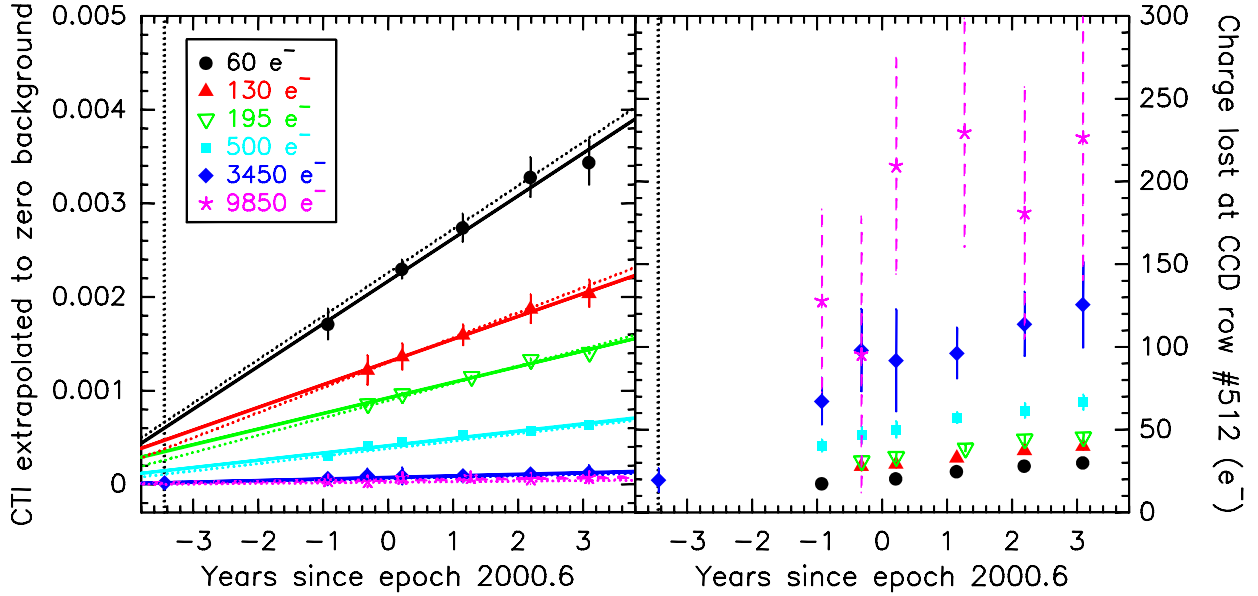


Fig. 6.— *Left panel:* CTI normalized to zero background for gain = 1 as a function of time and signal level, derived from the internal sparse field test. Symbols associated with the data of individual signal levels (corrected for CTI) are indicated in the legend. The solid lines represent linear fits to the data (one for each signal level), while the dotted lines represent the result of applying Eq. 7 to the data (one line per signal level group). *Right panel:* Absolute charge lost due to CTI for an object at the central row of the STIS CCD as a function of time and signal level. Symbol types are the same as in the left panel. The epoch of *HST* Servicing Mission 2 (during which STIS was installed on *HST*) is depicted as a black dotted vertical line.

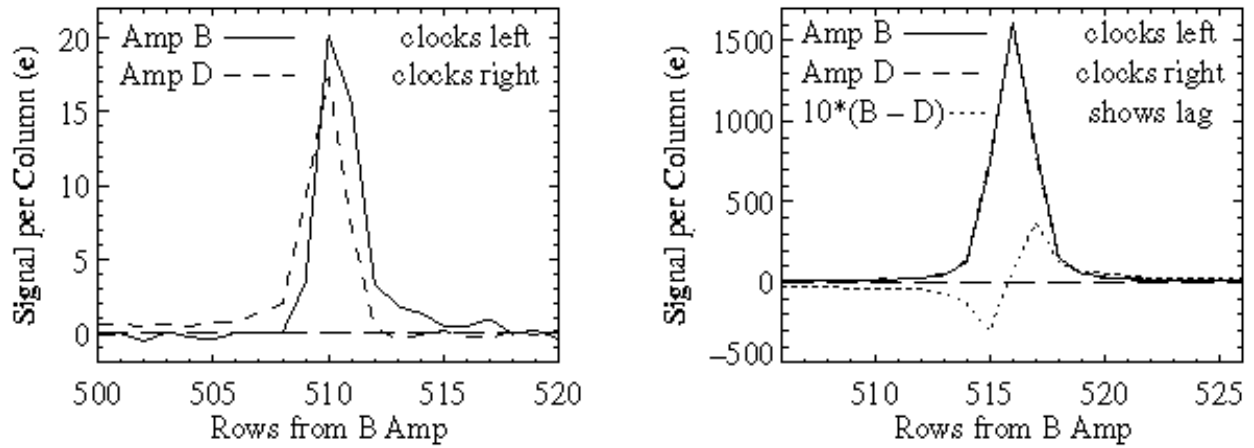


Fig. 7.— Comparison of line profiles obtained when clocking a given exposure in opposite directions in the internal sparse field test. At low signal levels (left panel), charge trailing and centroid shift are obvious. Even at high signal levels (right panel), differences in the line profile are systematic and measurable (the dotted line depicts the difference profile multiplied by 10). Figure reproduced from Kimble, Goudfrooij, & Gilliland (2000).

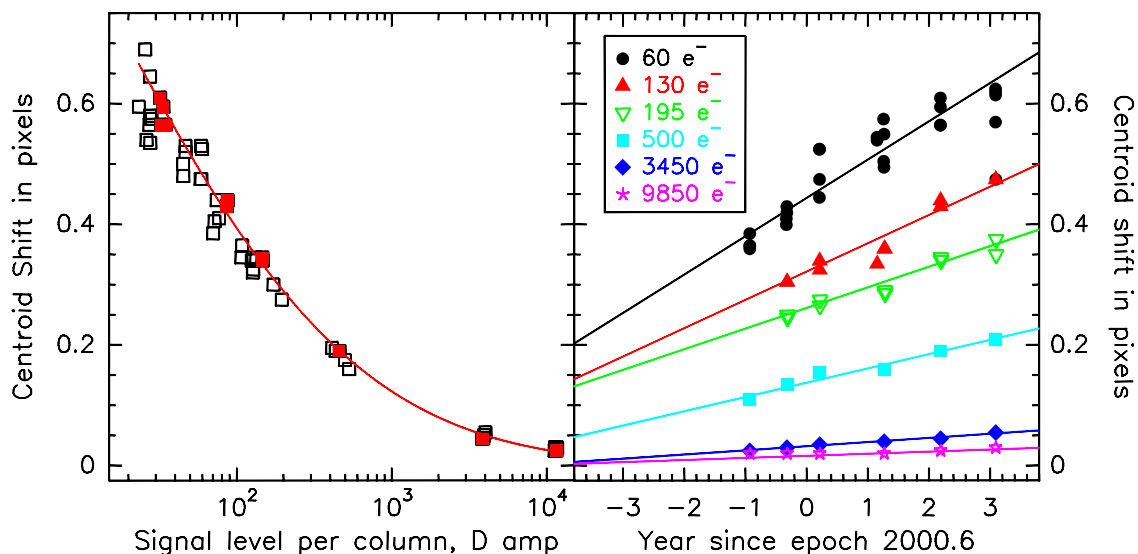


Fig. 8.— *Left panel:* The centroid shift (in unbinned CCD pixels) as a function of signal level as read out by the D amplifier for the gain = 1 observing block of the internal sparse field test in October 2002,  $\sim 5.5$  years after STIS installation. Centroid shifts for the central location on the CCD are shown in filled squares, and a least-squares fit to the latter is shown by the solid line. *Right panel:* The centroid shift for the central location on the CCD as functions of time and signal level as read out by the D amplifier. Both the data and the corresponding linear fits are plotted. Symbols associated with individual signal levels (corrected for CTI) are indicated in the legend.

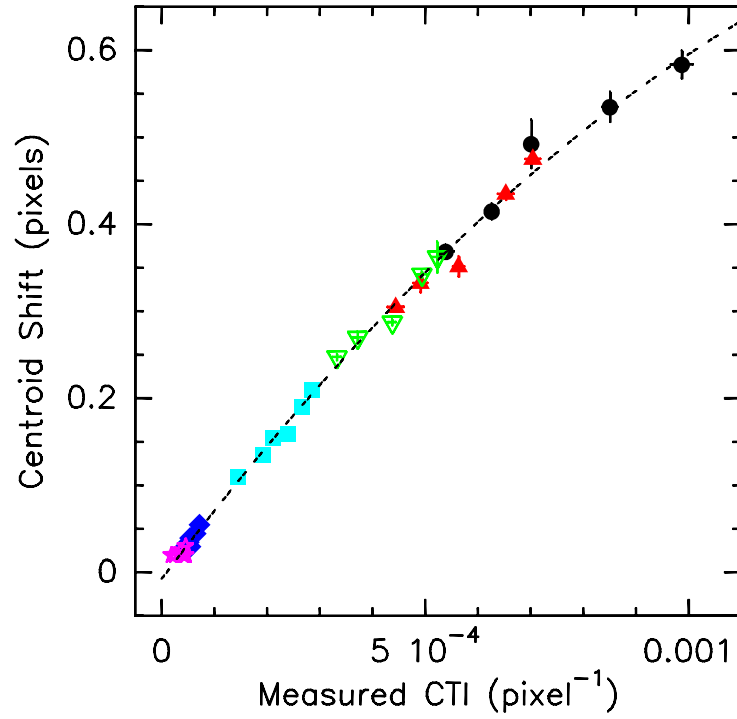


Fig. 9.— The centroid shift at the central row of the CCD as a function of CTI for all gain = 1 datasets of the internal sparse field test. Symbols as in Figure 8. Note the very tight relation between the two properties. A least-squares fit to the data (cf. Eq. 4) is shown by the dashed line.

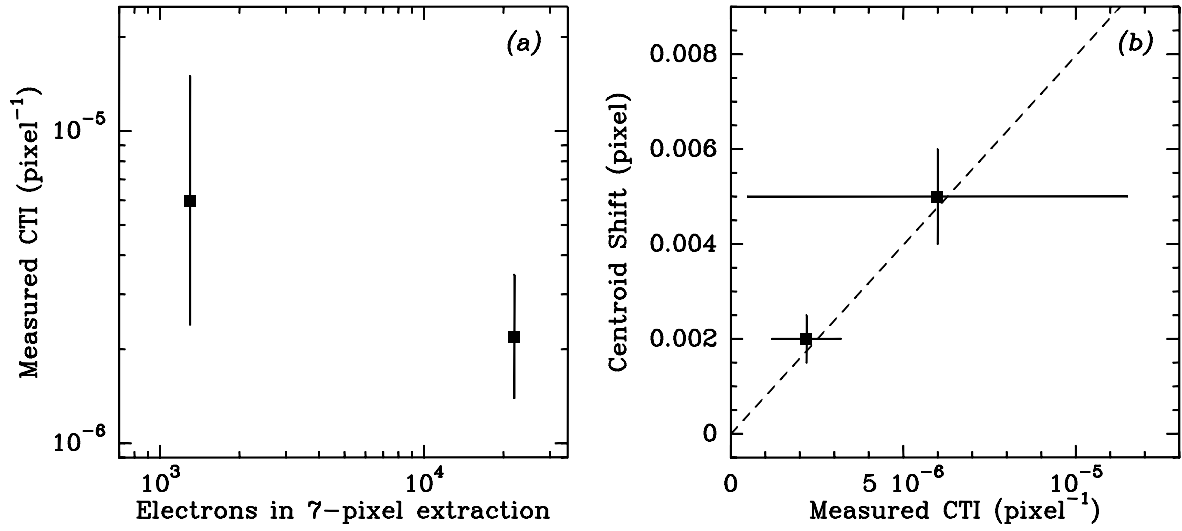


Fig. 10.— Panel (a): Serial CTI as a function of signal level for the 1999 epoch of the internal sparse field test. Panel (b): The centroid shift at the central column of the CCD as a function of CTI for the same data. The relation between CTI and centroid shift found for the parallel CTI (Eq. 4), as shown in Figure 9) is shown by the dashed line.

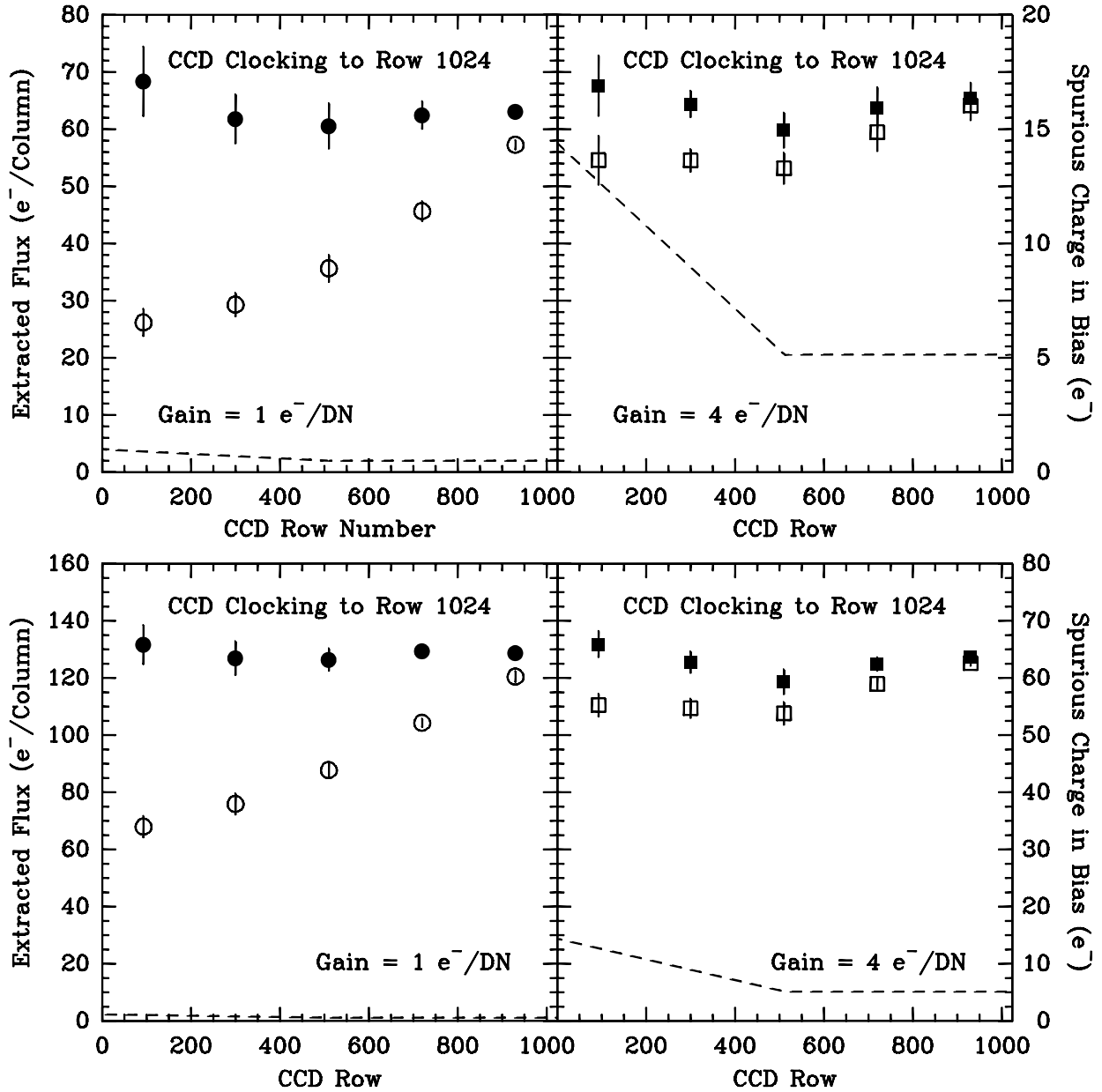


Fig. 11.— Results of the two lowest-signal cases of the 2002 epoch data of the internal sparse field test in the parallel clocking direction, for the two gain settings (1 and 4 e<sup>-</sup>/DN). The average signals measured at the five different positions along the CCD columns are shown as symbols (open circles for gain = 1 (left panels), open squares for gain = 4 (right panels)). Extracted signal levels are shown on the left-hand ordinate. The dashed lines depict the ‘background’ level due to spurious charge in STIS CCD superbias frames, averaged over all columns. Superbias intensity levels (in e<sup>-</sup> per pixel) are shown on the right-hand ordinates. Note the strong effect of local ‘background’ to the CTI for these low signal levels, especially for gain = 4 data. The latter show a much lower CTI than the gain = 1 data, due to a significantly higher amount of spurious charge in gain = 4. The filled symbols depict the signal levels after correction for CTI using Eqs. 7 and 10.



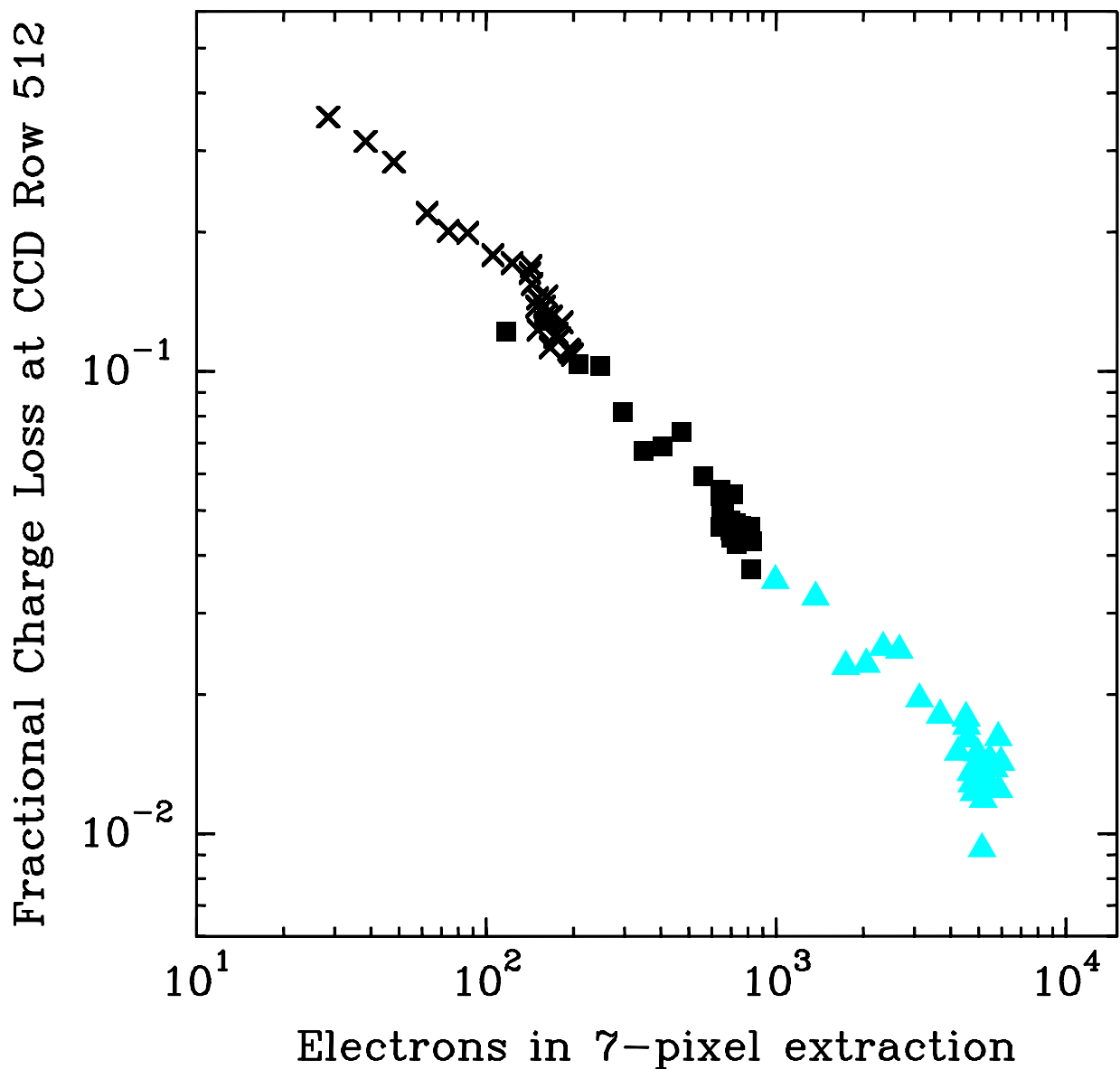


Fig. 12.— Fractional charge loss at the central row of the CCD (i.e.,  $(1 - \text{CTI})^{512}$ ) vs. extracted gross signal level for three G230LB wide-slit spectra of flux standard stars observed at the center of the STIS CCD. Crosses, squares, and triangles represent values for spectra o8v204030, 08v2040e0, and o6ig10010, respectively (see Table 5). The CTI values were normalized to correspond to epoch 2000.6 (see Sect. 3.1.1). Note the linear dependence of  $\log(\text{CTI})$  on  $\log(\text{signal level})$ .

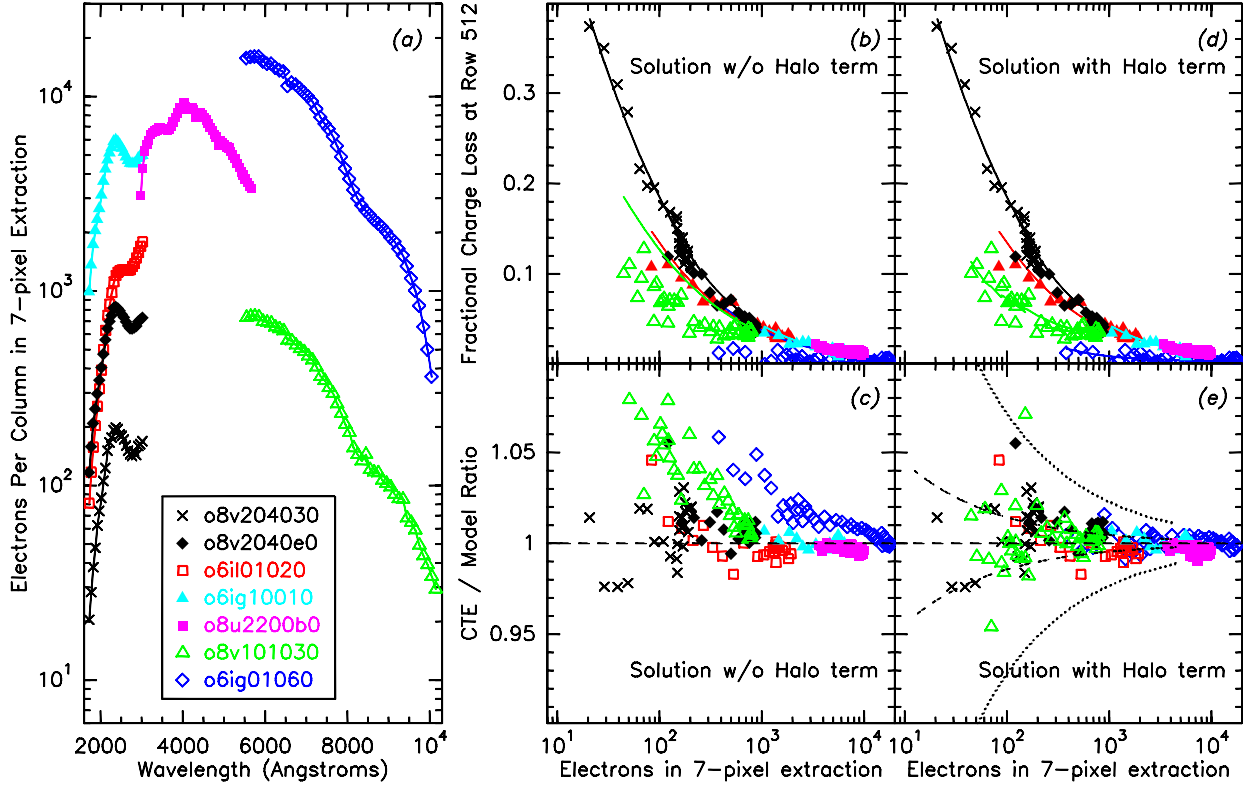
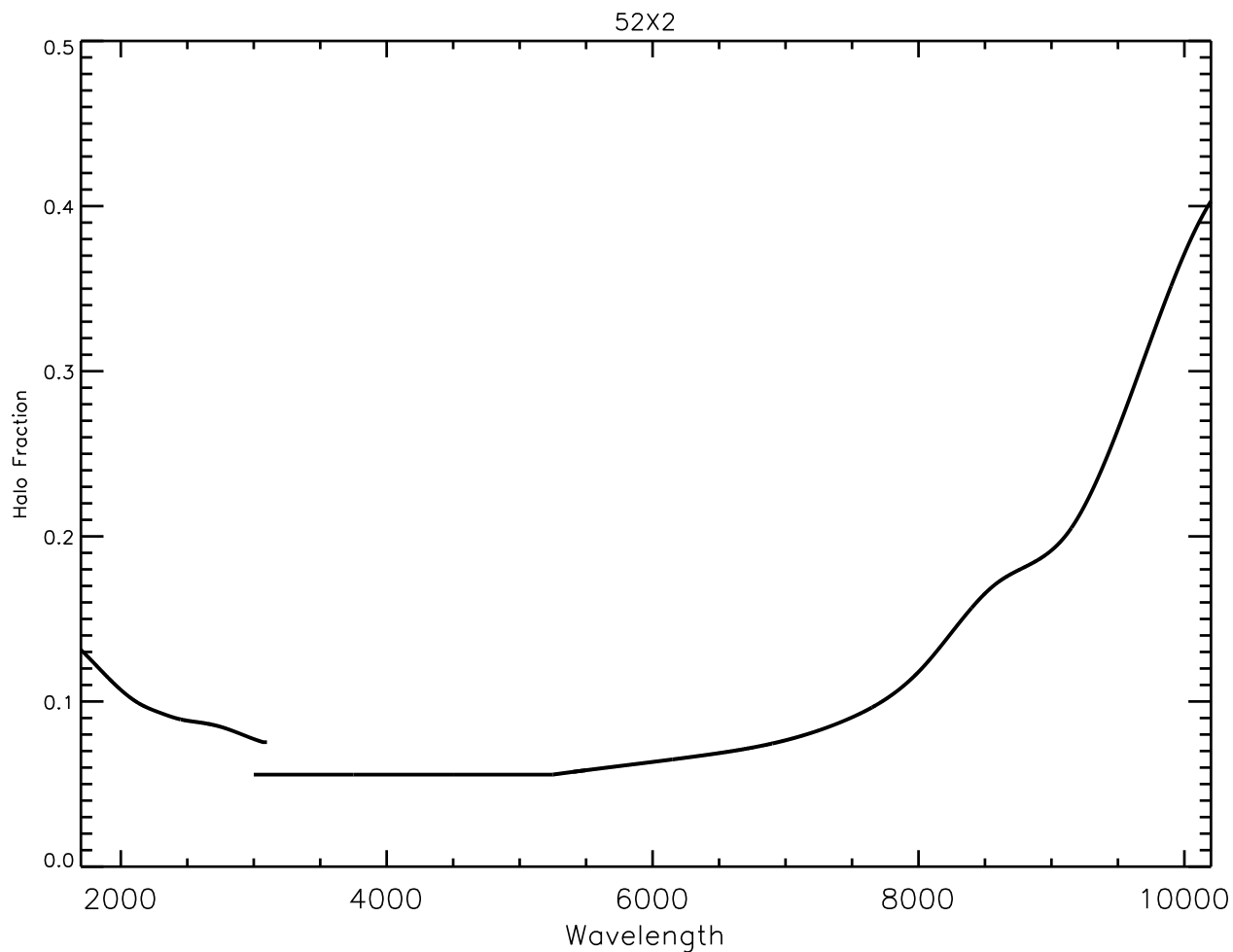


Fig. 13.— *Panel (a)*: Smoothed flux standard star spectra used to determine the functional form of the CTI of the STIS CCD in spectroscopic mode. The legend links the symbols with the STIS rootnames of the individual spectra, as listed in Table 5. *Panel (b)*: Fractional charge loss at the central row of the CCD vs. gross signal level within the default 7-pixel extraction box. Symbols represent measured CTI values for the spectra shown in panel (a), normalized to epoch 2000.6 (see Sect. 3.1.1). The smooth curves represent the predictions of the best-fit CTI model *without* ‘red halo’ term [i.e., Eq. 6] for those data. Symbol types are the same as in panel (a). *Panel (c)*: The ratio of measured CTE values and the model predictions shown in panel (b) vs. gross signal level. *Panel (d)*: Same as panel (b), but now using the final CTI model including a ‘red halo’ term [i.e., Eq. 7]. *Panel (e)*: Same as panel (c), but now using the final CTI model including a ‘red halo’ term. For reference, the dashed lines represent the uncertainty due to Poisson noise associated with the binned spectra shown in panel (a) as a function of signal level, while the dotted lines represent the Poisson error associated with a resolution element (2 pixels along the dispersion) of unbinned spectra.



Bohlin: INTERACTIVE 25-Oct-2005 14:11

Fig. 14.— Parameter  $H$  in Eq. 7: The fraction of the light in the PSF above the default 7-pixel extraction box as a function of wavelength for the STIS CCD grating modes. Note the discontinuity near  $3000 \text{ \AA}$ , at the boundary of the wavelength ranges covered by the G230LB and G430L gratings. This is likely due to the presence of a Lyot stop in the G430L and G750L modes which is absent in the G230LB mode (see also Dressel et al. 2006; Proffitt 2006).

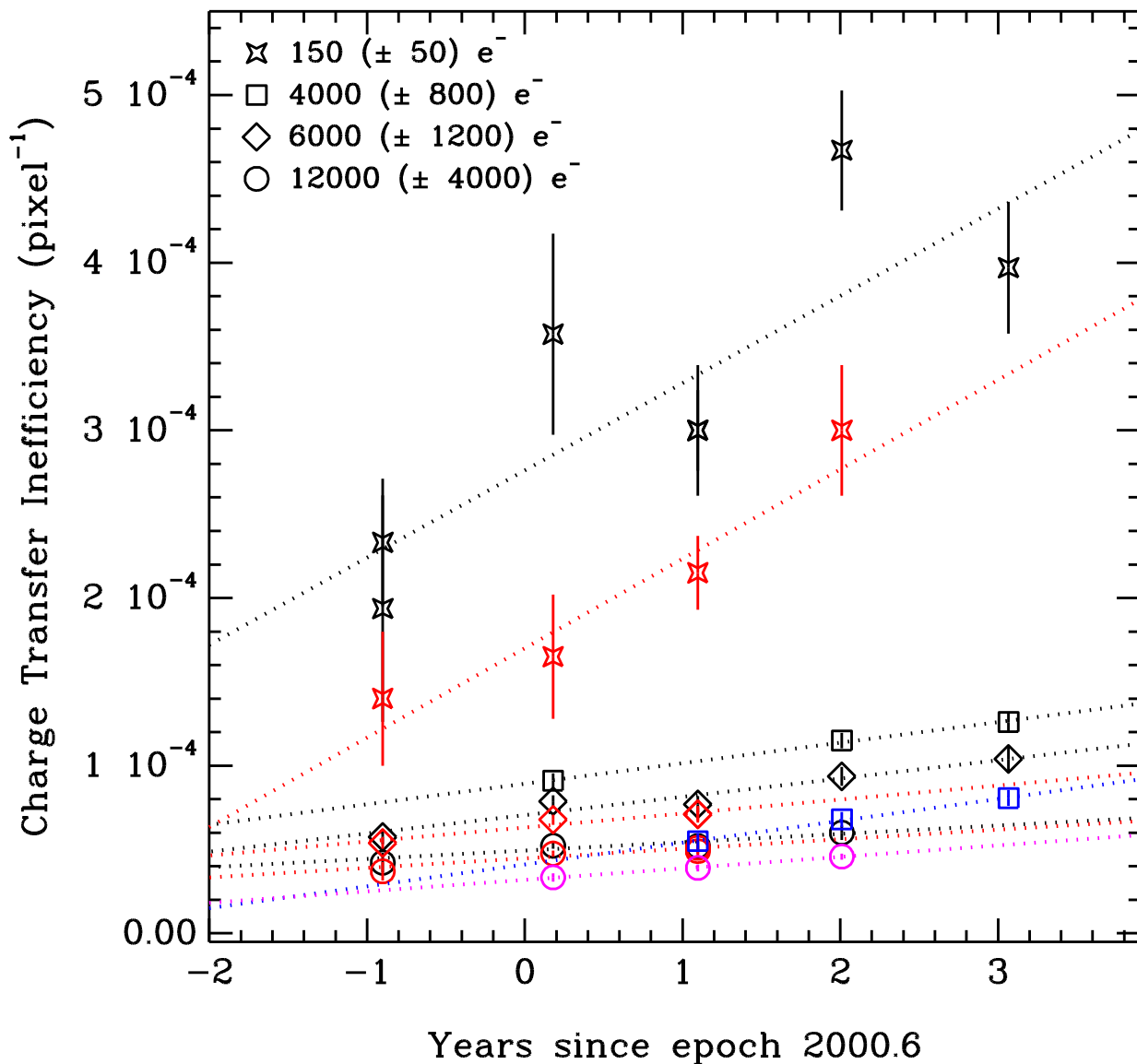


Fig. 15.— Imaging CTI as a function of time, derived from the external sparse field test. Both the data and the corresponding linear fits are plotted (the latter in dotted lines). Symbols associated with individual signal levels are indicated in the legend (at the top left). Data with different sky background have symbols with different colors: Black for sky =  $3 e^- \text{ pixel}^{-1}$ , red for sky =  $6 e^- \text{ pixel}^{-1}$ , blue for sky =  $10 e^- \text{ pixel}^{-1}$ , and magenta for sky =  $30 e^- \text{ pixel}^{-1}$ .

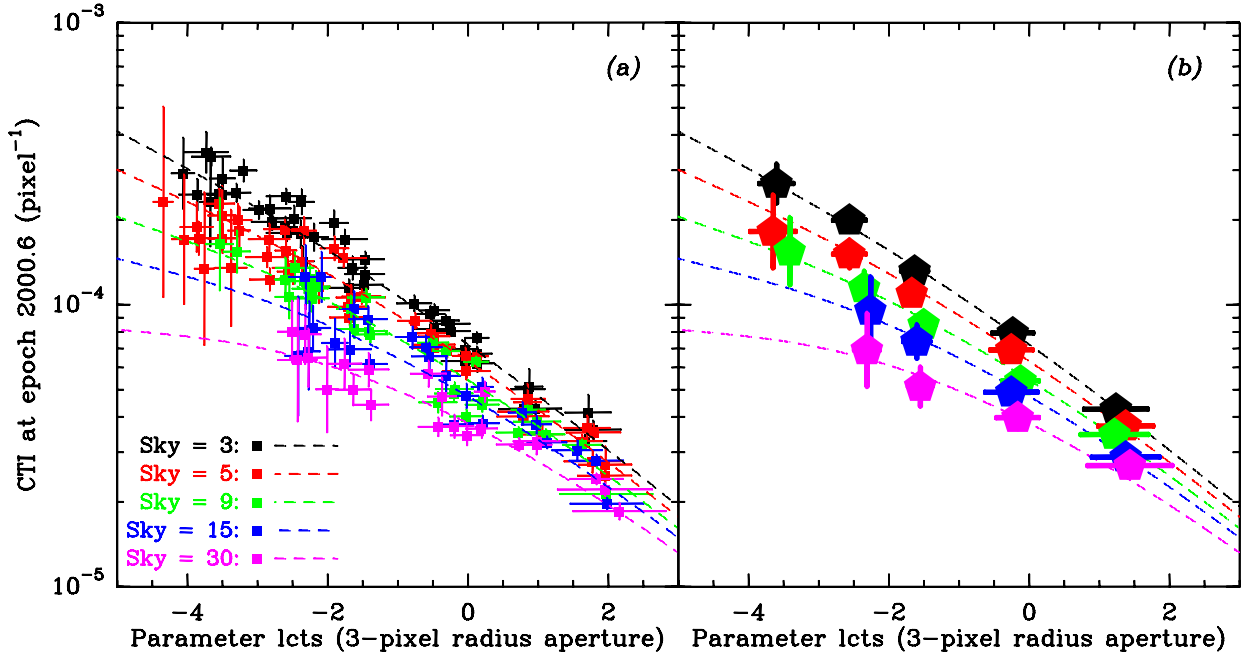


Fig. 16.— CTI at epoch 2000.6 as a function of parameter ‘lcts’ (as defined in Sect. 3.2.2) for imaging data derived from the external sparse field test. Panel (a) shows all individual data points listed in Table 7, while panel (b) shows *weighted mean* data points (averaged over 5 ranges of ‘lcts’, namely  $-3 < \text{lcts}$ ,  $-3 \leq \text{lcts} < -2$ ,  $-2 \leq \text{lcts} < -1$ ,  $-1 \leq \text{lcts} < 0.5$ , and  $\text{lcts} \geq 0.5$ , separately for each sky level). The drawn lines in both panels depict the fit of Eq. 8 to the data. Symbol and line colors associated with individual sky levels (in  $e^- \text{pixel}^{-1}$ ) are indicated in the legend in panel (a) (at the bottom left).

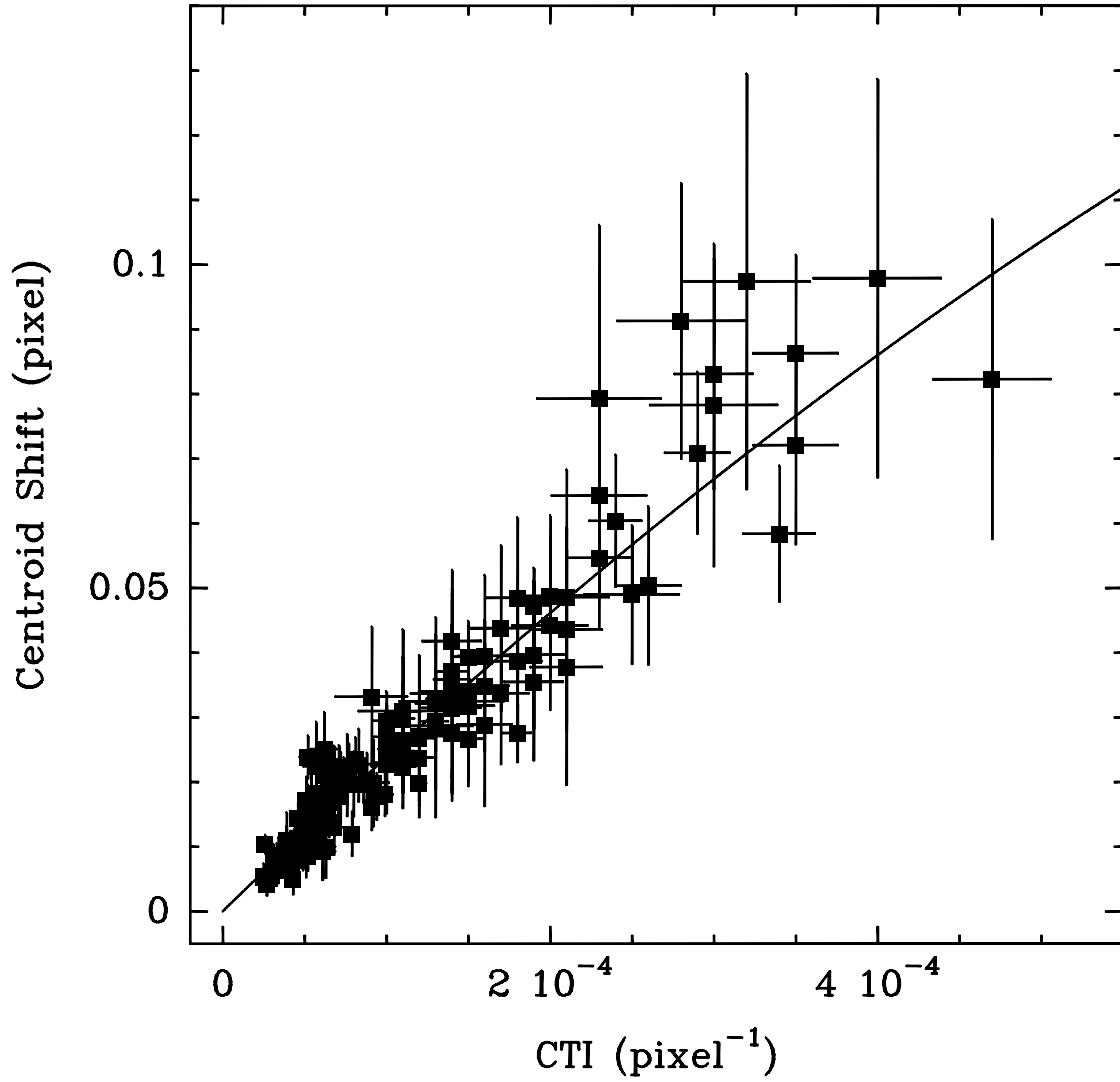


Fig. 17.— The centroid shift at the central row of the CCD as a function of CTI for the imaging data taken during the external sparse field tests. A weighted least-squares fit to the data (cf. Eq. 9) is shown by the solid line.

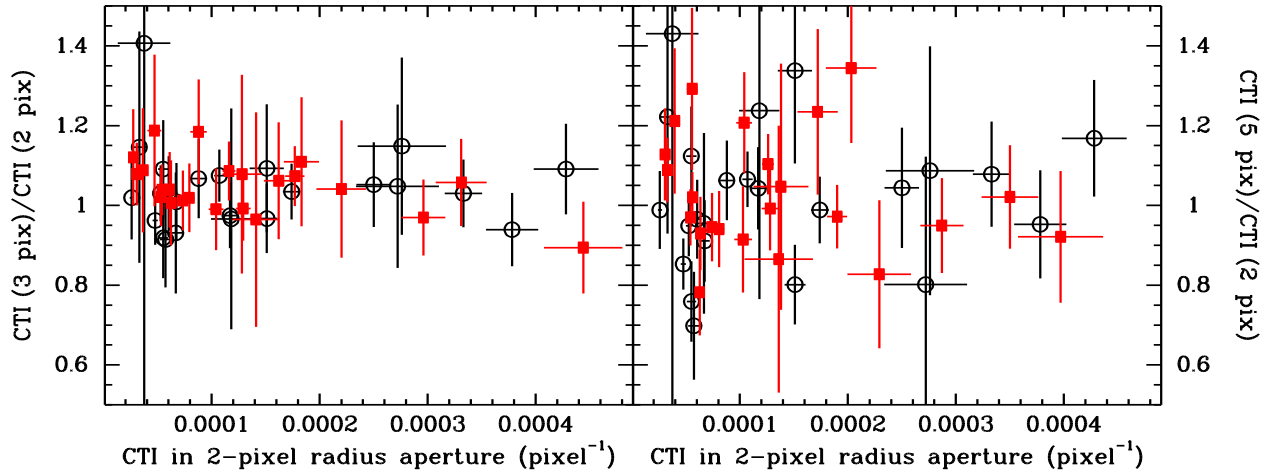


Fig. 18.— The ratio between imaging CTI values measured in different aperture sizes. *Left panel:* 3-pixel radius vs. 2-pixel radius. *Right panel:* 5-pixel radius vs. 2-pixel radius. Open circles indicate measurements from the Sep 2002 epoch, while filled squares indicate measurements from the Sep 2003 epoch. The size of the measurement aperture does not have any significant impact on the CTI in imaging mode.

Table 1. STIS observations for “internal” sparse field tests

Optical Element	$\lambda_{\text{cen}}$ (Å)	Slit Name	Exp. Time (s)	CCD Gain (e <sup>-</sup> /DN)	Signal Levels <sup>a</sup>
G430M	5471	0.05x31NDA	0.3	1, 4	60
G430M	5471	0.05x31NDA	0.6	1, 4	130
G430M	5471	0.05x31NDA	0.9	1, 4	195
G430M	5471	0.05x31NDA	2.3	1, 4	500
Mirror	— <sup>b</sup>	0.05x31NDA	0.3	1, 4	3400
Mirror	— <sup>b</sup>	0.05x31NDB	0.3	1, 4	9800

<sup>a</sup>Unit is e<sup>-</sup> per column *in the absence of CTE losses*.

<sup>b</sup>Using “Clear” filter (i.e., no filter; aperture name 50CCD)

Note. — All exposures were taken in two read modes: Once read out using the default amplifier “D”, and once using amplifier “B”, on the opposite side of the parallel register.

Table 2. Observing blocks used for the internal sparse field test. Each block extended over a time period of one to a few days. Representative values for the Modified Julian Date (MJD) and the civil date are shown.

Gain	Block	Program	MJD	Date (UT)
1	1	8414	51428	Sep 07, 1999
1	2	8414	51650	Apr 16, 2000
1	3	8851	51845	Oct 28, 2000
1	4	8910	52210	Oct 28, 2001
1	5	9620	52567	Oct 20, 2002
1	6	9620	52896	Sep 14, 2003
4	1	8414	51783	Aug 26, 2000
4	2	8851	52004	Apr 04, 2001
4	3	8910	52399	May 05, 2002
4	4	9620	52734	Apr 05, 2003
4	5	10026	53099	Apr 04, 2004



Table 3. STIS observations<sup>a</sup> for “external” sparse imaging field test

Observing Date	On-orbit Time (yr)	Exp. Time (s)	$N_{\text{exp}}$	CCD Gain ( $e^-/\text{DN}$ )	Background Levels <sup>b</sup>
Sep 15, 1999	2.54	20	24	1	3.1, 5.1
		100	9	1	14
Oct 13, 2000	3.62	20	40	1	3.3, 5.9, 7.9
		100	12	1	16, 27
Sep 13, 2001	4.54	20	40	1	3.0, 5.8, 7.9
		100	12	1	11, 37
Sep 13, 2002	5.45	20	40	1	2.9, 5.3
		100	12	1	11, 33
Sep 13, 2003	6.51	20	40	1	3.4
		100	12	1	11, 16

<sup>a</sup>The imaging field in NGC 6752 was centered on  $\alpha = 19^{\text{d}}11^{\text{m}}05^{\text{s}}96$ ,  $\delta = -60^{\circ}01'06''7$  in J2000 equinox. Observations were conducted using the “Clear” filter (i.e., no filter; aperture name 50CCD).

<sup>b</sup>Centroids of histogram of sky pixel values windowed to  $\pm 4\sigma$  of the mean. Unit is  $e^-$  per pixel.

Note. — All exposures were taken in two read modes: Once read out using the default amplifier “D”, and once using amplifier “B”, on the opposite side of the parallel register. Celestial coordinates are given in equinox J2000.

Table 4: CTI time constant  $\alpha$  as measured from the internal sparse field test data taken in gain = 1, as a function of signal level.

signal (DN)	$\alpha$ ( $\text{yr}^{-1}$ )	$\sigma_{\alpha}$ ( $\text{yr}^{-1}$ )
60	0.216	0.009
130	0.192	0.013
195	0.188	0.021
500	0.202	0.016
3450	0.218	0.038
9850	0.170	0.052

Table 5: List of flux standard star spectra used to characterize the CTI as function of signal and background level. All intensities are in  $e^-$  per pixel per (sub-)exposure.

Rootname	Grating	Flux Standard	Observing Date	Background level	Range in Signal Levels
o6ig10010	G230LB	G191 – B2B	2002-04-22	0.4	1000 – 5000
o6ig01060	G750L	GD 71	2001-12-07	1.7	300 – 16000
o6i101020	G230LB	LDS 749B	2001-07-13	1.9	100 – 1800
o8u2200b0	G430L	AGK+81D266	2003-11-03	0.5	3000 – 9200
o8v101030	G750L	WD 1657+343	2004-04-07	2.5	30 – 750
o8v2040e0	G230LB	GD 71	2003-10-24	0.3	120 – 730
o8v204030	G230LB	GD 71	2003-10-24	0.1	20 – 170

Table 6: Best-fit Values of Coefficients in Functional Form of Spectroscopic CTI (Eq. 7).

Coefficient	Value	Description
$\alpha$	$0.056 \pm 0.001$	CTI normalization
$\beta$	$0.82 \pm 0.01$	Gross count level dependence
$\gamma$	$0.205 \pm 0.006$	Time dependence of CTI
$\delta$	$3.00 \pm 0.05$	Multiplicative factor for ‘background’/gross count ratio
$\epsilon$	$1.30 \pm 0.10$	Multiplicative factor for halo light fraction
$\zeta$	$0.18 \pm 0.01$	Power of ‘background’/gross count ratio
$\eta$	$0.06 \pm 0.01$	Minimum value of halo light fraction above spectrum

Table 7: Measured CTI values and centroid shifts for external sparse imaging field test data.

MJD	Sky Level ( $e^-/\text{pixel}$ )	Signal Level ( $e^-$ )	CTI ( $\text{pixel}^{-1}$ )	Centroid Shift (pixel)
51436	3.1	$149 \pm 27$	$(2.3 \pm 0.4) 10^{-4}$	$0.0793 \pm 0.0268$
	3.1	$293 \pm 87$	$(1.8 \pm 0.2) 10^{-4}$	$0.0485 \pm 0.0124$
	3.1	$460 \pm 82$	$(1.9 \pm 0.2) 10^{-4}$	$0.0397 \pm 0.0114$
	3.1	$852 \pm 276$	$(1.4 \pm 0.1) 10^{-4}$	$0.0359 \pm 0.0084$
	3.1	$2293 \pm 567$	$(8.3 \pm 0.5) 10^{-5}$	$0.0226 \pm 0.0056$
	3.1	$2888 \pm 593$	$(7.6 \pm 0.5) 10^{-5}$	$0.0211 \pm 0.0063$
	3.1	$4708 \pm 913$	$(5.7 \pm 0.4) 10^{-5}$	$0.0183 \pm 0.0070$
	5.1	$290 \pm 85$	$(1.4 \pm 0.2) 10^{-4}$	$0.0418 \pm 0.0110$
	5.1	$476 \pm 84$	$(1.5 \pm 0.2) 10^{-4}$	$0.0318 \pm 0.0115$
	5.1	$836 \pm 274$	$(1.2 \pm 0.1) 10^{-4}$	$0.0268 \pm 0.0073$
	5.1	$2320 \pm 569$	$(7.2 \pm 0.4) 10^{-5}$	$0.0192 \pm 0.0055$
	5.1	$2902 \pm 587$	$(6.5 \pm 0.4) 10^{-5}$	$0.0182 \pm 0.0053$
	5.1	$4765 \pm 876$	$(5.4 \pm 0.4) 10^{-5}$	$0.0158 \pm 0.0060$
	14.1	$915 \pm 279$	$(5.7 \pm 0.8) 10^{-5}$	$0.0225 \pm 0.0068$
	14.1	$2231 \pm 532$	$(6.3 \pm 0.6) 10^{-5}$	$0.0100 \pm 0.0048$
	14.1	$4833 \pm 838$	$(3.9 \pm 0.4) 10^{-5}$	$0.0111 \pm 0.0042$
	14.1	$10721 \pm 2157$	$(3.4 \pm 0.3) 10^{-5}$	$0.0086 \pm 0.0028$
	14.1	$23397 \pm 8367$	$(2.5 \pm 0.2) 10^{-5}$	$0.0055 \pm 0.0019$
51831	3.3	$413 \pm 101$	$(2.1 \pm 0.2) 10^{-4}$	$0.0436 \pm 0.0157$
	3.3	$951 \pm 193$	$(1.4 \pm 0.1) 10^{-4}$	$0.0276 \pm 0.0069$
	3.3	$1141 \pm 308$	$(1.5 \pm 0.1) 10^{-4}$	$0.0267 \pm 0.0073$
	3.3	$3055 \pm 659$	$(9.9 \pm 0.5) 10^{-5}$	$0.0181 \pm 0.0033$
	3.3	$3586 \pm 689$	$(9.1 \pm 0.4) 10^{-5}$	$0.0161 \pm 0.0035$
	3.3	$5600 \pm 957$	$(7.9 \pm 0.4) 10^{-5}$	$0.0120 \pm 0.0034$
	3.3	$11594 \pm 2812$	$(5.2 \pm 0.2) 10^{-5}$	$0.0086 \pm 0.0023$
	3.3	$26075 \pm 8100$	$(3.4 \pm 0.2) 10^{-5}$	$0.0072 \pm 0.0028$
	5.9	$407 \pm 119$	$(1.4 \pm 0.2) 10^{-4}$	$0.0340 \pm 0.0158$
	5.9	$931 \pm 195$	$(1.1 \pm 0.1) 10^{-4}$	$0.0309 \pm 0.0084$
	5.9	$1156 \pm 315$	$(1.1 \pm 0.1) 10^{-4}$	$0.0265 \pm 0.0076$
	5.9	$3049 \pm 675$	$(8.0 \pm 0.4) 10^{-5}$	$0.0197 \pm 0.0050$
	5.9	$3661 \pm 689$	$(7.1 \pm 0.4) 10^{-5}$	$0.0179 \pm 0.0053$
	5.9	$5585 \pm 925$	$(6.8 \pm 0.3) 10^{-5}$	$0.0169 \pm 0.0052$
	5.9	$11666 \pm 2821$	$(4.8 \pm 0.2) 10^{-5}$	$0.0116 \pm 0.0048$

Table 7: (continued)

MJD	Sky Level ( $e^-/\text{pixel}$ )	Signal Level ( $e^-$ )	CTI ( $\text{pixel}^{-1}$ )	Centroid Shift (pixel)
51831	7.9	$417 \pm 113$	$(1.4 \pm 0.2) 10^{-4}$	$0.0315 \pm 0.0128$
	7.9	$930 \pm 183$	$(1.0 \pm 0.1) 10^{-4}$	$0.0228 \pm 0.0076$
	7.9	$1153 \pm 303$	$(1.1 \pm 0.1) 10^{-4}$	$0.0224 \pm 0.0064$
	7.9	$3007 \pm 661$	$(7.6 \pm 0.4) 10^{-5}$	$0.0199 \pm 0.0034$
	7.9	$3622 \pm 691$	$(7.1 \pm 0.4) 10^{-5}$	$0.0180 \pm 0.0032$
	7.9	$5546 \pm 945$	$(6.5 \pm 0.3) 10^{-5}$	$0.0138 \pm 0.0023$
	7.9	$11656 \pm 2819$	$(4.4 \pm 0.2) 10^{-5}$	$0.0104 \pm 0.0019$
	7.9	$25093 \pm 6925$	$(3.3 \pm 0.1) 10^{-5}$	$0.0067 \pm 0.0020$
	14.8	$1188 \pm 325$	$(9.2 \pm 0.1) 10^{-5}$	$0.0199 \pm 0.0067$
	14.8	$2846 \pm 718$	$(6.8 \pm 0.8) 10^{-5}$	$0.0130 \pm 0.0042$
	14.8	$3604 \pm 742$	$(5.8 \pm 0.9) 10^{-5}$	$0.0144 \pm 0.0046$
	14.8	$6047 \pm 937$	$(5.3 \pm 0.4) 10^{-5}$	$0.0139 \pm 0.0037$
	14.8	$13100 \pm 2780$	$(3.9 \pm 0.3) 10^{-5}$	$0.0103 \pm 0.0029$
	14.8	$30780 \pm 11882$	$(2.9 \pm 0.1) 10^{-5}$	$0.0052 \pm 0.0017$
	29.5	$1197 \pm 344$	$(6.1 \pm 0.8) 10^{-5}$	$0.0169 \pm 0.0058$
	29.5	$2809 \pm 714$	$(5.9 \pm 0.6) 10^{-5}$	$0.0137 \pm 0.0040$
	29.5	$3403 \pm 696$	$(4.9 \pm 0.8) 10^{-5}$	$0.0124 \pm 0.0049$
	29.5	$6268 \pm 917$	$(5.1 \pm 0.4) 10^{-5}$	$0.0091 \pm 0.0038$
	29.5	$13111 \pm 2866$	$(3.3 \pm 0.3) 10^{-5}$	$0.0087 \pm 0.0018$
	29.5	$30806 \pm 11776$	$(2.5 \pm 0.1) 10^{-5}$	$0.0054 \pm 0.0012$
52166	3.0	$148 \pm 30$	$(3.0 \pm 0.2) 10^{-4}$	$0.0831 \pm 0.0178$
	3.0	$302 \pm 88$	$(2.4 \pm 0.2) 10^{-4}$	$0.0604 \pm 0.0102$
	3.0	$904 \pm 253$	$(1.4 \pm 0.1) 10^{-4}$	$0.0371 \pm 0.0069$
	3.0	$3031 \pm 882$	$(1.0 \pm 0.1) 10^{-4}$	$0.0251 \pm 0.0036$
	3.0	$4739 \pm 1598$	$(7.7 \pm 0.5) 10^{-5}$	$0.0224 \pm 0.0036$
	3.0	$10969 \pm 3939$	$(5.2 \pm 0.3) 10^{-5}$	$0.0147 \pm 0.0049$
	3.0	$29354 \pm 11702$	$(4.4 \pm 0.3) 10^{-5}$	$0.0091 \pm 0.0036$
	5.8	$149 \pm 30$	$(2.1 \pm 0.3) 10^{-4}$	$0.0486 \pm 0.0197$
	5.8	$281 \pm 84$	$(1.8 \pm 0.2) 10^{-4}$	$0.0387 \pm 0.0108$
	5.8	$893 \pm 254$	$(1.2 \pm 0.1) 10^{-4}$	$0.0238 \pm 0.0066$
	5.8	$3046 \pm 901$	$(8.8 \pm 0.4) 10^{-5}$	$0.0202 \pm 0.0043$
	5.8	$4811 \pm 1612$	$(7.1 \pm 0.5) 10^{-5}$	$0.0197 \pm 0.0060$

Table 7: (continued)

MJD	Sky Level ( $e^-/\text{pixel}$ )	Signal Level ( $e^-$ )	CTI ( $\text{pixel}^{-1}$ )	Centroid Shift (pixel)	
52166	7.9	$149 \pm 31$	$(2.1 \pm 0.2) 10^{-4}$	$0.0378 \pm 0.0182$	
	7.9	$292 \pm 83$	$(1.5 \pm 0.1) 10^{-4}$	$0.0341 \pm 0.0100$	
	7.9	$912 \pm 255$	$(1.1 \pm 0.1) 10^{-4}$	$0.0248 \pm 0.0054$	
	7.9	$3042 \pm 901$	$(8.6 \pm 0.3) 10^{-5}$	$0.0197 \pm 0.0029$	
	7.9	$4812 \pm 1620$	$(7.1 \pm 0.4) 10^{-5}$	$0.0188 \pm 0.0033$	
	7.9	$10801 \pm 4001$	$(4.9 \pm 0.3) 10^{-5}$	$0.0103 \pm 0.0039$	
	7.9	$29533 \pm 11383$	$(4.3 \pm 0.3) 10^{-5}$	$0.0050 \pm 0.0023$	
	11.4	$385 \pm 76$	$(1.3 \pm 0.2) 10^{-4}$	$0.0287 \pm 0.0141$	
	11.4	$977 \pm 236$	$(1.0 \pm 0.1) 10^{-4}$	$0.0230 \pm 0.0060$	
	11.4	$3217 \pm 867$	$(5.5 \pm 0.5) 10^{-5}$	$0.0130 \pm 0.0032$	
	11.4	$4818 \pm 1126$	$(4.9 \pm 0.3) 10^{-5}$	$0.0098 \pm 0.0032$	
	11.4	$10145 \pm 3215$	$(4.3 \pm 0.2) 10^{-5}$	$0.0085 \pm 0.0020$	
	11.4	$35503 \pm 23516$	$(2.6 \pm 0.2) 10^{-5}$	$0.0054 \pm 0.0019$	
	35.2	$960 \pm 235$	$(6.1 \pm 0.8) 10^{-5}$	$0.0093 \pm 0.0044$	
	35.2	$3225 \pm 905$	$(4.5 \pm 0.4) 10^{-5}$	$0.0084 \pm 0.0036$	
	35.2	$4864 \pm 1139$	$(4.2 \pm 0.4) 10^{-5}$	$0.0077 \pm 0.0026$	
	35.2	$10218 \pm 3289$	$(3.9 \pm 0.2) 10^{-5}$	$0.0064 \pm 0.0025$	
	35.2	$34799 \pm 23530$	$(2.7 \pm 0.1) 10^{-5}$	$0.0042 \pm 0.0017$	
	52499	2.9	$127 \pm 35$	$(4.7 \pm 0.4) 10^{-4}$	$0.0823 \pm 0.0247$
		2.9	$182 \pm 37$	$(3.5 \pm 0.3) 10^{-4}$	$0.0721 \pm 0.0153$
2.9		$369 \pm 103$	$(3.4 \pm 0.2) 10^{-4}$	$0.0584 \pm 0.0105$	
2.9		$1131 \pm 321$	$(1.8 \pm 0.1) 10^{-4}$	$0.0276 \pm 0.0045$	
2.9		$3833 \pm 1076$	$(1.2 \pm 0.5) 10^{-4}$	$0.0198 \pm 0.0034$	
2.9		$5610 \pm 1198$	$(9.4 \pm 0.6) 10^{-5}$	$0.0178 \pm 0.0036$	
2.9		$12893 \pm 4821$	$(6.0 \pm 0.4) 10^{-5}$	$0.0140 \pm 0.0056$	
5.3		$185 \pm 37$	$(2.8 \pm 0.4) 10^{-4}$	$0.0913 \pm 0.0213$	
5.3		$362 \pm 108$	$(2.6 \pm 0.2) 10^{-4}$	$0.0504 \pm 0.0122$	
5.3		$461 \pm 76$	$(2.0 \pm 0.2) 10^{-4}$	$0.0488 \pm 0.0124$	
5.3		$1082 \pm 297$	$(1.5 \pm 0.1) 10^{-4}$	$0.0394 \pm 0.0055$	
11.0		$520 \pm 132$	$(1.6 \pm 0.2) 10^{-4}$	$0.0349 \pm 0.0101$	
11.0		$1226 \pm 305$	$(1.1 \pm 0.1) 10^{-4}$	$0.0298 \pm 0.0054$	
11.0		$4029 \pm 1095$	$(6.8 \pm 0.5) 10^{-5}$	$0.0225 \pm 0.0031$	
11.0		$6037 \pm 1438$	$(6.2 \pm 0.4) 10^{-5}$	$0.0165 \pm 0.0029$	
11.0		$13224 \pm 4429$	$(5.4 \pm 0.3) 10^{-5}$	$0.0128 \pm 0.0025$	

Table 7: (continued)

MJD	Sky Level ( $e^-/\text{pixel}$ )	Signal Level ( $e^-$ )	CTI ( $\text{pixel}^{-1}$ )	Centroid Shift (pixel)
52499	32.6	$483 \pm 111$	$(1.1 \pm 0.3) 10^{-4}$	$0.0310 \pm 0.0126$
	32.6	$507 \pm 133$	$(9.1 \pm 0.2) 10^{-5}$	$0.0332 \pm 0.0108$
	32.6	$1237 \pm 312$	$(6.2 \pm 0.8) 10^{-5}$	$0.0251 \pm 0.0057$
	32.6	$4067 \pm 1108$	$(5.2 \pm 0.5) 10^{-5}$	$0.0239 \pm 0.0033$
	32.6	$5986 \pm 1344$	$(5.1 \pm 0.4) 10^{-5}$	$0.0173 \pm 0.0035$
	32.6	$13158 \pm 4413$	$(4.6 \pm 0.2) 10^{-5}$	$0.0145 \pm 0.0022$
	32.6	$42713 \pm 8317$	$(2.6 \pm 0.2) 10^{-5}$	$0.0104 \pm 0.0014$
52885	3.4	$141 \pm 27$	$(4.0 \pm 0.4) 10^{-4}$	$0.0979 \pm 0.0308$
	3.4	$250 \pm 55$	$(3.5 \pm 0.3) 10^{-4}$	$0.0863 \pm 0.0152$
	3.4	$372 \pm 107$	$(2.9 \pm 0.2) 10^{-4}$	$0.0709 \pm 0.0125$
	3.4	$468 \pm 75$	$(2.3 \pm 0.3) 10^{-4}$	$0.0643 \pm 0.0153$
	3.4	$1118 \pm 310$	$(1.9 \pm 0.1) 10^{-4}$	$0.0473 \pm 0.0058$
	3.4	$3862 \pm 1061$	$(1.3 \pm 0.1) 10^{-4}$	$0.0329 \pm 0.0043$
	3.4	$5630 \pm 1207$	$(1.0 \pm 0.1) 10^{-4}$	$0.0270 \pm 0.0050$
	3.4	$14176 \pm 4217$	$(5.6 \pm 0.5) 10^{-5}$	$0.0145 \pm 0.0038$
	3.4	$34584 \pm 13298$	$(4.0 \pm 0.3) 10^{-5}$	$0.0085 \pm 0.0031$
	11.3	$517 \pm 74$	$(2.0 \pm 0.2) 10^{-4}$	$0.0442 \pm 0.0130$
	11.3	$1212 \pm 305$	$(1.3 \pm 0.1) 10^{-4}$	$0.0294 \pm 0.0046$
	11.3	$4077 \pm 1100$	$(8.1 \pm 0.5) 10^{-5}$	$0.0236 \pm 0.0033$
	11.3	$6155 \pm 1432$	$(7.4 \pm 0.4) 10^{-5}$	$0.0204 \pm 0.0034$
	11.3	$15001 \pm 4020$	$(5.6 \pm 0.2) 10^{-5}$	$0.0134 \pm 0.0019$
	11.3	$35832 \pm 18767$	$(3.3 \pm 0.2) 10^{-5}$	$0.0076 \pm 0.0015$
	15.5	$540 \pm 137$	$(1.4 \pm 0.3) 10^{-4}$	$0.0337 \pm 0.0153$
	15.5	$1213 \pm 304$	$(1.0 \pm 0.1) 10^{-4}$	$0.0295 \pm 0.0045$
	15.5	$4064 \pm 1084$	$(6.3 \pm 0.5) 10^{-5}$	$0.0211 \pm 0.0039$
	15.5	$6086 \pm 1416$	$(6.3 \pm 0.4) 10^{-5}$	$0.0176 \pm 0.0036$
	15.5	$15225 \pm 4272$	$(5.4 \pm 0.3) 10^{-5}$	$0.0139 \pm 0.0021$
15.5	$37163 \pm 18658$	$(3.1 \pm 0.2) 10^{-5}$	$0.0082 \pm 0.0022$	

Table 8: Best-fit Values of Coefficients in Functional Form of Imaging CTI (Eq. 8).

Coefficient	Value	Description
$a$	$(1.33 \pm 0.03) 10^{-4}$	CTI normalization
$b$	$0.54 \pm 0.01$	Count level dependence
$c$	$0.205 \pm 0.006$	Time dependence of CTI
$d$	$0.05 \pm 0.02$	Fraction of dependence on background (vs. background/flux ratio)
$e$	$0.82 \pm 0.05$	Multiplicative factor for background level dependence
$f$	$3.60 \pm 0.07$	Multiplicative factor of background/flux count ratio dependence
$g$	$0.21 \pm 0.02$	Power of background/flux count ratio